

# Alongstream, seasonal and interannual variability of the North Icelandic Irminger Current and East Icelandic Current around Iceland

M. Casanova-Masjoan<sup>1</sup>, M.D Pérez-Hernández<sup>1,2</sup>, R.S. Pickart<sup>3</sup>, H. Valdimarsson<sup>2</sup>, A. Macrander<sup>2</sup>, D. Grisolia-Santos<sup>1</sup>, D. J. Torres<sup>3</sup>, S. Jonsson<sup>2,4</sup>, K. Våge<sup>5</sup>, A. Hernández-Guerra<sup>1</sup>

<sup>1</sup>Unidad océano y clima, Instituto de Oceanografía y Cambio Global, IOCAG, Universidad de Las Palmas de Gran Canaria, ULPGC, Unidad Asociada ULPGC-CSIC, Las Palmas de Gran Canaria, Spain.

<sup>2</sup>Marine and Freshwater Research Institute, Reykjavík, Iceland.

<sup>3</sup>Department of Physical Oceanography, Woods Hole Oceanographic Institution, Woods Hole, Massachusetts, USA.

<sup>4</sup>University of Akureyri, Akureyri, Iceland.

<sup>5</sup>Geophysical Institute, University of Bergen and Bjerknes Centre for Climate Research, Bergen, Norway.

Corresponding author: Maria Casanova-Masjoan ([maria.casanova102@alu.ulpgc.es](mailto:maria.casanova102@alu.ulpgc.es))

## Key Points:

- The NIIC merges with the EIC north of Iceland forming a single current that continues flowing around Iceland without loss of transport.
- The percentage of AW within the NIIC is higher than 75% until it merges with the EIC, after which the AtOW percentage is higher.
- Over the 25-year period, the NIIC has become warmer, saltier and its transport has increased.

## Abstract

Data from repeat hydrographic surveys over the 25-year period 1993 to 2017, together with satellite altimetry data, are used to quantify the temporal and spatial variability of the North Icelandic Irminger Current (NIIC), East Icelandic Current (EIC), and the water masses they advect around northern Iceland. We focus on the warm, salty Atlantic Water (AW) flowing northward through Denmark Strait, and the cooler, fresher, denser Atlantic-origin Overflow Water (AtOW) which has circulated cyclonically around the rim of the Nordic Seas before being advected to the Iceland slope via the EIC. The absolute geostrophic velocities reveal that some portion of the NIIC recirculates just north of Denmark Strait, while the remaining portion merges with the EIC to form a single current that extends to the northeast of Iceland, with no further loss in transport of either component. The AW percentage decreases by 75% over this distance, while the AtOW percentage is higher than that of the AW in the merged current. A seasonal accounting of the water masses within the currents indicates that only in springtime is the NIIC dominated by AW north of Denmark Strait. In the remaining seasons other water masses contribute significantly. Overall, there is considerably more seasonal and alongstream variability in the properties of the flow prior to the merging of the NIIC and EIC. Over the 25-year time period, the NIIC has become warmer, saltier, and has increased in volume transport. On interannual timescales, some of the variability can be related to established climate indices.

## Plain Language Summary

In the Nordic Seas, warm water emanating from the sub-tropical North Atlantic Ocean is converted to cold, dense water through wintertime heat loss to the atmosphere. This warm-to-cold transformation, and the subsequent transport of the dense water back to the North Atlantic, is part of the “Meridional Overturning Circulation” which helps regulate Earth’s climate. In this study we investigate the evolution, variability, and fate of the warm water that flows northward through Denmark Strait, between Greenland and Iceland, using a set of shipboard transects collected over 25 years along with satellite data. The current is known as the North Icelandic Irminger Current (NIIC). We demonstrate that part of the NIIC recirculates just north of the strait, and the remaining part is joined by another current stemming from the East Greenland slope, known as the East Icelandic Current (EIC). Originally the NIIC and EIC flow side by side, but then merge into a single current that flows to the northeast part of Iceland. The water in the NIIC and merged flow becomes progressively colder and fresher, but there is no loss in transport. Over the 25-year period the NIIC has become warmer, saltier, and its transport has increased.

## 1 Introduction

The inflow of relatively warm and saline Atlantic Water (AW) northward across the Greenland-Scotland Ridge is a fundamental component of the Atlantic Meridional Overturning Circulation (AMOC). North of the ridge, wintertime heat loss to the atmosphere densifies the water, transforming it into overflow water that eventually flows back southward into the deep North Atlantic Ocean. The largest global warming rates are occurring at high latitudes (Blunden & Arndt, 2016), and the regions around the Arctic Ocean have been warming two times faster than the global average. The AW inflow to the Nordic Seas has warmed 1.4°C since 1980 (Oziel et al., 2016). At the same time, the AW inflow varies strongly in temperature, salinity and

transport on seasonal to multi-decadal time scales (Behrens et al., 2017; Latarius & Quadfasel, 2016 and Zhao et al., 2018).

The penetration of warm water across the Greenland-Scotland Ridge takes place along three different pathways: through Denmark Strait, between Iceland and the Faroe Islands, and through the Faroe-Shetland Channel (Hansen & Østerhus, 2000). The latter two branches flow northward through the Norwegian Sea where significant densification takes place (Mauritzen, 1996). At Fram Strait, a substantial portion of the dense AW retroflects and combines with the outflow from the Arctic Ocean to form the East Greenland Current (EGC, Fig. 1). This flow is also joined by AW exiting the western side of the strait that had previously been modified in the Arctic Ocean. The two types of transformed AW are together referred to as Atlantic-origin Overflow Water (AtOW; e.g. Håvik et al., 2017). Some portion of these waters flow into Denmark Strait and participate in the overflow plume that enters the Irminger Sea, forming the headwaters of the Deep Western Boundary Current. The composite pathway and modification of AW encircling the perimeter of the Nordic Seas from southeast Norway to Denmark Strait is known as the rim current overturning loop (Mauritzen, 1996).

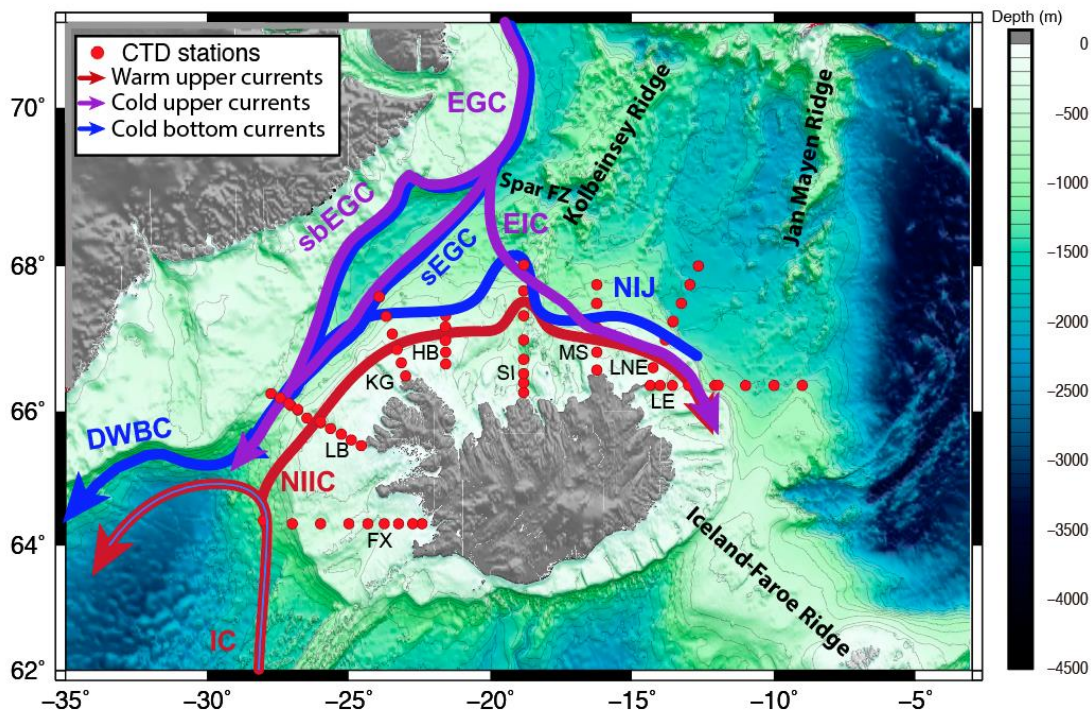


**Figure 1:** Schematic representation of the main currents in the vicinity of Iceland: NIIC = North Icelandic Irminger Current; IC = Irminger Current; DWBC = Deep Western Boundary Current; EGC = East Greenland Current; sbEGC = shelfbreak EGC; sEGC = separated EGC; EIC = East Iceland Current; and NIJ = North Icelandic Jet. The hydrographic stations used in this study are indicated by the red circles, comprising 8 transects: FX = Faxaflói, LB = Látrabjarg, KG = Kögur, HB = Hornbanki, SI = Siglunes, MS = Melrakkslétta, LNE = Langanes NE, and LE = Langanes E. The bathymetry is from the GEBCO\_2014 grid. Major topographic features are labeled.

The evolution and fate of the third branch of warm AW, entering the Nordic Seas on the eastern side of Denmark Strait, is less certain (Fig. 1). The origin of this water is the Irminger Current which flows northward on the western side of the Reykjanes Ridge (Bersch, 1995; McCartney & Talley, 1982). South of Denmark Strait the majority of this AW recirculates (Bersch, 1995; Kristmannsson, 1998; Pickart et al., 2005; Logemann et al., 2013) and

subsequently flows equatorward along the East Greenland shelf break. The remaining portion flows northward into the Iceland Sea as the North Icelandic Irminger Current (Logemann & Harms, 2006) (NIIC, Fig. 1), with a small contribution from an inner coastal branch. Transport estimates of the NIIC range from 0.95 Sv (Jonsson & Briem, 2003) to 3.4 Sv (Krauss, 1995) ( $1 \text{ Sv} = 10^6 \text{ m}^3 \text{ s}^{-1}$ ). More recently, Jonsson & Valdimarsson (2012b) calculated a transport of 0.88 Sv using 16 years of mooring data on the northwest Iceland shelf at the Hornbanki section. It must be noted, however, that this value represents “pure” AW, which was defined using an end-member approach. Using this same methodology, (Pickart et al., 2017a) computed a transport of 1.71 Sv of pure AW based on 6 absolutely referenced geostrophic velocity sections from specific times at the Kögur section somewhat west of the Hornbanki section.

In contrast to the AW that participates in the rim current overturning loop, it is presently unknown exactly where and how the AW in the NIIC contributes to the overturning circulation of the Nordic Seas. Using an idealized numerical model, Våge et al. (2011) hypothesized that the NIIC represents the upper limb of a local overturning cell in the Iceland Sea. In their model, the NIIC sheds much/most of its water offshore via the formation of eddies as it flows along the north slope of Iceland, essentially disintegrating. The warm water fluxed seaward is subsequently densified by air-sea heat loss in the central Iceland Sea before returning southward and sinking along the continental slope. The model indicated that this sinking forms a significant portion of the North Icelandic Jet (NIJ) which is known to advect Arctic-origin Overflow Water (ArOW) into the eastern side of Denmark Strait (Harden et al., 2016; Steingrímur Jonsson & Valdimarsson, 2004; Pickart et al., 2017a; Semper et al., 2019; Våge et al., 2011, 2013; Zhao et al., 2018). The ArOW is colder, fresher, and denser than the AtOW, and it constitutes the remaining part of the overflow plume entering the Irminger Sea. However, in contrast to the model of Våge et al. (2011), a correspondence between the disintegration of the NIIC and alongstream evolution of the NIJ is not supported by hydrographic/velocity surveys north of Iceland (Semper et al., 2019).

While there is additional support for a central Iceland Sea overturning loop (Behrens et al., 2017; Pickart et al., 2017a), a number of studies have now cast doubt on some aspects of this scheme. This includes the fact that the densest and deepest wintertime mixed layers are found to the northwest of the Iceland Sea gyre, and even this transformed water can't account for the densest portion of the NIJ (Våge et al., 2015). Furthermore, numerical models suggest that very little of the NIIC water returns through Denmark Strait as overflow water (Ypma et al., 2019). Other models indicate that the NIJ stems from waters emanating far to the north, flowing along topographic ridges into the Iceland Sea (Köhl et al., 2007; Yang & Pratt, 2014).

Another aspect of the regional circulation north of Iceland that appears to factor into the fate of AW entering Denmark Strait is the East Icelandic Current (EIC). This current is believed to branch off of the EGC roughly 500 km north of Denmark Strait and flow to the southeast on the southern side of the Iceland Sea Gyre (Jónsson, 2007). It advects a combination of Polar Surface Water (Rudels et al., 2005), Iceland Sea Arctic Intermediate Water (Macrandar et al., 2014), and AtOW from the EGC. In the vicinity of northeast Iceland, the EIC meets the NIIC and the two currents flow side by side (Macrandar et al., 2014). However, it remains unclear to what degree the composite flow is comprised of the NIIC versus the EIC (although this seems to vary in time; Macrandar et al., 2014). Ultimately the combined flow is believed to progress into the Norwegian Sea (de Jong et al., 2018).

In addition to its possible role in the overturning circulation of the Nordic Seas, the AW inflow through Denmark Strait helps govern the climate of Iceland and also impacts the uptake of CO<sub>2</sub> in the Iceland Sea (Hamilton et al., 2004). To date, however, there have been limited studies addressing the full extent of the NIIC. The drifter study of Valdimarsson & Malmberg (1999) suggested that much of the current is detrained in the vicinity of the Kolbeinsey Ridge. In particular, the majority of the drifters passing through Denmark Strait in the current recirculated west of the ridge and flowed back into the strait. On the other hand, data from shipboard sections indicate a significant presence of the NIIC in the vicinity of the shelfbreak northeast of Iceland (Hermansen, 2012). This is supported by different model studies in which the NIIC is present all along the north slope of Iceland, although its strength varies seasonally and interannually (Logemann et al., 2013; Ypma et al., 2019; Zhao et al., 2018). At the same time, the models of Behrens et al. (2017) and Ypma et al. (2019) suggest that at least some portion of the NIIC contributes to local overturning in the Iceland Sea.

The aim of this study is to quantify the spatial, seasonal and interannual variability of the AW inflow through Denmark Strait as well as the currents flowing along Iceland's shelf and slope, i.e. the NIIC and the EIC. Changes in the hydrographic properties and volume transport of the flow during the last 25 years will be explored using in-situ and satellite data from 1993 to 2017. The variability will then be assessed in light of different climatic indices. The study is divided into the following parts. In section 2, we describe the data and methods, which includes the use of potential temperature and salinity data from shipboard sections as well as altimetry data. The different climatic indices are also explained. Section 3 addresses the alongstream variation of the mean state, including a presentation of the volume transports. Section 4 investigates the vorticity characteristics of the flow. Section 5 describes the seasonal variability, and Section 6 addresses the interannual variability and explores ways that this is related to the climatic indices. We finish with a summary of the results.

## 2 Data and Methods

### 2.1 Shipboard data

The hydrographic data used in this study come from the seasonal shipboard surveys around the western and northern Iceland shelf and slope, occupied by the Marine and Freshwater Research Institute of Iceland (MFRI). Progressing clockwise around Iceland, the surveys consist of the following sections (Fig. 1): Faxaflói (FX) west of Iceland; Látrabjarg (LB) and Kögur (KG) in Denmark Strait; Hornbanki (HB); Siglunes (SI); Melrakkaslétta (MS); and, finally, Langanes Northeast (LNE) and Langanes East (LE) northeast of Iceland. We use the data from the surveys carried out between February 1993 and October 2017, which corresponds to the period of altimetric data coverage.

All of the cruises include conductivity-temperature-depth (CTD) measurements, obtained with a Sea-Bird 911+ instrument mounted on a rosette with Niskin bottles. Salinity samples were collected at selected depths in order to perform an in-situ calibration of the conductivity sensor. Based on this information and the laboratory calibrations, the instrument accuracies are estimated to be 0.3 db, 0.001°C, and 0.002 for pressure, temperature, and practical salinity, respectively (see Våge et al. (2011)).

A subset of the cruises included Lower Acoustic Doppler Current Profiler (LADCP) measurements. These were the surveys carried out in August 2009 and 2015, and February 2011, 2012 and 2013. The LADCP system consisted of dual (upward and downward facing) 300 kHz Workhorse ADCPs from Teledyne, RD Instruments. These were internally recording units powered from an external rechargeable battery pack. The instruments were set up to collect 16 8-meter bins of single ping data at 1 Hz continuously throughout each cast. The raw data were processed to remove the motion of the CTD package and the ship using the LADCP Processing Software Package from the Lamont-Doherty Earth Observatory (Thurnherr, 2018). Comparisons between downcast and upcast measurements, as well as shear standard deviation calculations made during data processing, were used to determine uncertainty in the LADCP measurements (Thurnherr, 2010; Visbeck, 2002). A regional high resolution (1/60 degree) implementation of the Oregon State University global inverse barotropic tidal model (Egbert et al., 1994; Egbert & Erofeeva, 2002) was used to remove the barotropic tidal component from the LADCP velocities. Errors from the tidal model were primarily due to errors in the bathymetry used by the tidal model. The resulting uncertainty in the velocity, due to instrument measurement error and inaccuracies in the tidal model, is  $\pm 3$  cm/s (Våge et al., 2011).

The sections are comprised of standard stations that are occupied on most cruises, except in a few cases of poor weather conditions. The typical station spacing is  $\sim 10$  km over the shelf and  $\sim 20$  km offshore of the shelfbreak. The number of cruises used per season and transects in this study are summarized in Table 1. The winter season is defined as January, February and March; spring is April, May and June; summer is July, August and September; and fall is October November and December. The final hydrographic data set consists of vertical sections of potential temperature, salinity, and potential density for each of the eight transects occupied from 1993 to 2017. The sections were constructed using Laplacian-Spline interpolation (see Pickart (1992)) with a grid spacing of 10 km in the horizontal and 10 m in the vertical.

**Table 1:** Number of cruises per transect and season used in the study.

	Winter	Spring	Summer	Fall	total
Faxaflói	21	25	18	22	86
Látrabjarg	12	15	15	15	57
Kögur	16	17	23	16	72
Hornbanki	19	19	13	18	69
Siglunes	20	22	24	19	85
Melrakkaslétta	0	14	4	2	20
Langanes NE	23	27	25	21	96
Langanes E	16	23	15	9	63
Total	127	162	137	122	548

## 2.2 Altimetry data

Daily Absolute Dynamic Topography (ADT) data from altimetry were obtained from AVISO database (<https://www.aviso.altimetry.fr/en/home.html>) for the region spanning 10–30°W and 62–70°N. This product contains gridded surface geostrophic velocity data which are

used to reference the relative geostrophic velocity from the hydrographic data. The ADT product combines data from different altimeter missions, computed with respect to a 20-year mean. Of all the missions used in this product, only ENVISAT reaches latitudes north of 66°N (see <http://volkov.oce.orst.edu>).

There are several challenges and potential errors associated with the use of altimetry in our study area. Ducet et al. (2000) and Le Traon et al. (1998) found significant mapping errors in the region of the Greenland shelf due to the presence of sea ice. Another challenge is the poor sampling near coastal areas. The swath of the altimeter is very narrow, thus when the satellite is traveling in a specific orbit this results in inter-track gaps that are unsampled (Vignudelli et al., 2006). A third issue is the relatively small spatial scales of the currents in the region, although satellite altimetry data have been used successfully in these circumstances. For example, Ruiz Etcheverry et al. (2015) compared annual cycles of sea level anomaly from altimetry to that determined from tide gauges, and found a root mean square difference of smaller than 2 cm for the majority of the cases. We assess the accuracy of the altimetry data along the MFRI transects listed above using the LADCP observations in section 2.4.

### 2.3 Wind data and Ekman transport

Wind data from the ERA-Interim reanalysis produced by the European Centre for Medium-Range Weather Forecast (ECMWF), as described in Dee et al. (2011), are used to estimate Ekman transports for each survey. This is done using the wind-stress interpolated to the location between each station pair where the geostrophic velocity is estimated. In general, Ekman transports are in the range -0.25 to 0.25 Sv, except for transect FX where they reached between -0.5 and 0.5 Sv during several surveys.

### 2.4 Absolute geostrophic velocities and transports

Relative geostrophic velocities for each station pair are estimated from the geopotential anomaly referenced to the sea surface. Absolute geostrophic velocities are then computed by adjusting the initial profiles based on the surface geostrophic velocity from the altimetry data product. In particular, the altimeter-derived velocities are interpolated to the location between each station pair. These values are then compared to the mean of the upper 20 m of the corresponding relative geostrophic velocity profile in order to determine the reference velocity.

The LADCP data collected on the subset of cruises allowed for assessment of the altimeter-derived surface geostrophic velocity in the study area. For the transects with LADCP data, we estimated the reference velocities by averaging the cross-track LADCP profiles for each station pair and choosing the depth interval where the LADCP shear and geostrophic velocity shear are similar (Comas-Rodríguez et al., 2010). Regressing the altimeter-derived reference velocities against the LADCP-derived reference velocities for each transect resulted in statistically significant correlations at all of the locations except for MS and LNE on the northeast side of Iceland. As such, absolute geostrophic velocities are only considered at the transects FX, LB, KG, HB, SI and LE.

Volume transports at these six lines are computed from the interpolated absolute geostrophic velocity sections. The Ekman transport is added to the first 100m of the volume transports. The sign convention used is that positive velocities and transports correspond to currents flowing clockwise around Iceland, while negative velocities and transports are associated with counterclockwise flow around Iceland.

## 2.5 Climatic Indices

Three climatic indices – the North Atlantic Oscillation, the Atlantic Multidecadal Oscillation, and the Greenland Blocking Index – are used to assess possible sources of the property and transport variability of the NIIC and EIC. The indices are obtained from the National Centers for Environmental Prediction (NCEP) project from the National Oceanic and Atmospheric Administration (NOAA, <https://www.esrl.noaa.gov>). The North Atlantic Oscillation and Greenland Blocking Index have been obtained as daily averaged data (Hanna et al., 2013), and the Atlantic Multidecadal Oscillation has been downloaded as monthly means (Enfield et al., 2001). Annual time series of the three indices have been used to estimate correlations and lags with the currents.

## 3 Water masses and alongstream characterization of the NIIC and EIC

We begin by identifying the different water masses present in the set of hydrographic sections around Iceland, which are listed in Table 2. We follow the property definitions of Rudels et al. (2005) and Våge et al. (2011). A volumetric potential temperature–salinity ( $\theta$ - $S$ ) diagram of all the data shows that most of the water in the occupations falls within three main water types (Fig. 2a). The primary focus of our study is the warm and salty AW transported northward by the NIIC (Jónsson & Valdimarsson, 2012b; 2012a; Swift & Aagaard, 1981; Våge et al., 2013). The most abundant water mass in the data set is the ArOW which is formed by winter convection in the Greenland and Iceland Seas (Våge et al., 2011). We do not consider this intermediate water mass in our study. The next abundant water mass is the AtOW that is advected southward in the EGC (Håvik et al., 2017; Rudels et al., 2005), some of which gets diverted to the region north of Iceland by the EIC (Rudels et al., 2005).

**Table 2:** Water masses definitions following Rudels et al. (2005) and Våge et al. (2011).

Water mass	Acronym	Definition of properties
Surface Water	SW	$T > 3^{\circ}\text{C}$ $\sigma_0 < 27.70 \text{ kg/m}^3$
warm Polar Surface Water	PSWw	$0 \leq T < 3^{\circ}\text{C}$ $\sigma_0 < 27.70 \text{ kg/m}^3$
Polar Surface Water	PSW	$T < 0^{\circ}\text{C}$ $\sigma_0 < 27.70 \text{ kg/m}^3$
Atlantic Water	AW	$T \geq 3^{\circ}\text{C}$ $S > 34.9$
Atlantic-origin Overflow Water	AtOW	$0 \leq T < 3^{\circ}\text{C}$ $\sigma_0 \geq 27.70 \text{ kg/m}^3$ $\sigma_{0.5} < 30.44 \text{ kg/m}^3$ $T < 0^{\circ}\text{C}$
Polar intermediate Water	PIW	$\sigma_0 \geq 27.70 \text{ kg/m}^3$ $S \leq 34.676$ $T < 0^{\circ}\text{C}$
Arctic-origin Overflow Water	ArOW	$\sigma_0 \geq 27.70 \text{ kg/m}^3$ $\sigma_{0.5} < 30.44 \text{ kg/m}^3$ $T < 0^{\circ}\text{C}$
Nordic Seas Deep Water	NDW	$\sigma_{0.5} \geq 30.44 \text{ kg/m}^3$



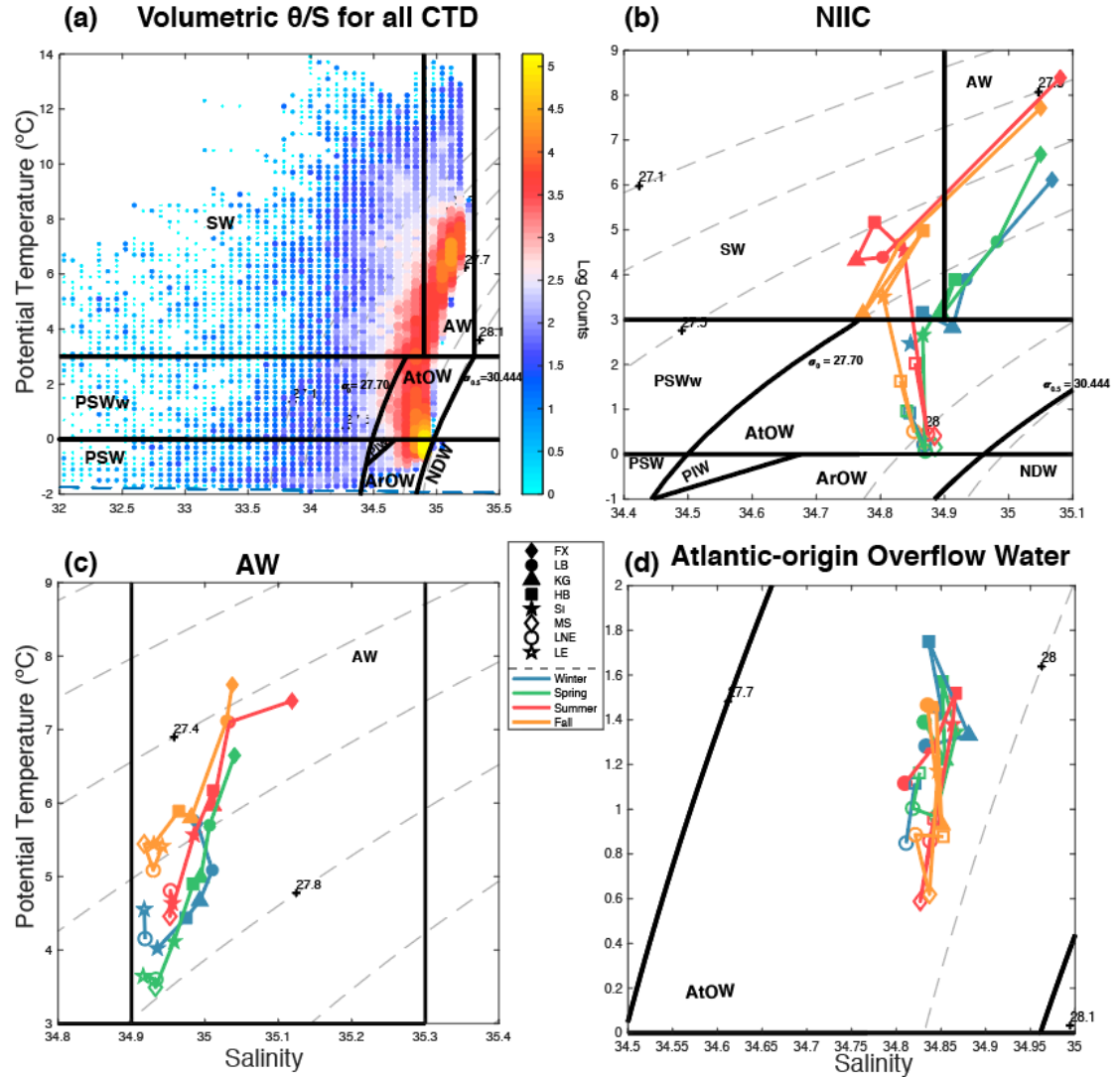


**Figure 2:** (a) Volumetric  $\theta$ -S diagram of all CTD stations, where color denotes the number of measurements within each bin of 0.2°C in temperature and 0.07 in salinity. The domains of the different water masses defined in Table 2 are denoted by the thick black lines. The acronyms are given in Table 2. (b) Seasonally averaged  $\theta$ -S of the NIIC and NIIC-EIC merged flow (color) per transect (symbols). See the legend. (c) Seasonally averaged  $\theta$ -S of the AW within the current. (d) Same as (c) except for AtOW. Grey dashed lines are the potential density ( $\text{kg m}^{-3}$ ).

The remaining water masses in the region are present in smaller amounts. The Polar Intermediate Water (PIW) which is thought to come from the Arctic thermocline (Rudels et al., 2005). Cold and fresh Polar Surface Water (PSW) is transported southward by the EGC and is mixed with the AW within Denmark Strait along the front formed by the EGC and the NIIC (Behrens et al., 2017; Latarius & Quadfasel, 2016; Logemann & Harms, 2006 and Zhao et al., 2018). Warm Polar Surface Water (SPWw) is formed by melting sea ice mixing with warm Atlantic Water (Rudels et al., 2005). Finally, Surface Water (SW) is characterized by a broad range in potential temperature and salinity due to the interaction with the atmosphere and also with fresh water intrusions from land.

The mean vertical sections of hydrographic properties for all 8 transects are shown in Figs. 3 and 4. Warm and salty subtropical-origin water is found south of Denmark Strait on the FX line, some of which enters the strait, although it is more confined to the shelf at the LB line. From here the water becomes steadily colder and fresher progressing around Iceland. However, even at the LE line there is a signature of this subtropical-origin water. At the edge of the warm and salty water there is a density front in all of the sections from Denmark Strait to northeast Iceland. The front is mainly dictated by temperature, and the resulting downward tilting isopycnals towards the shelf are associated with a substantial thermal wind shear.

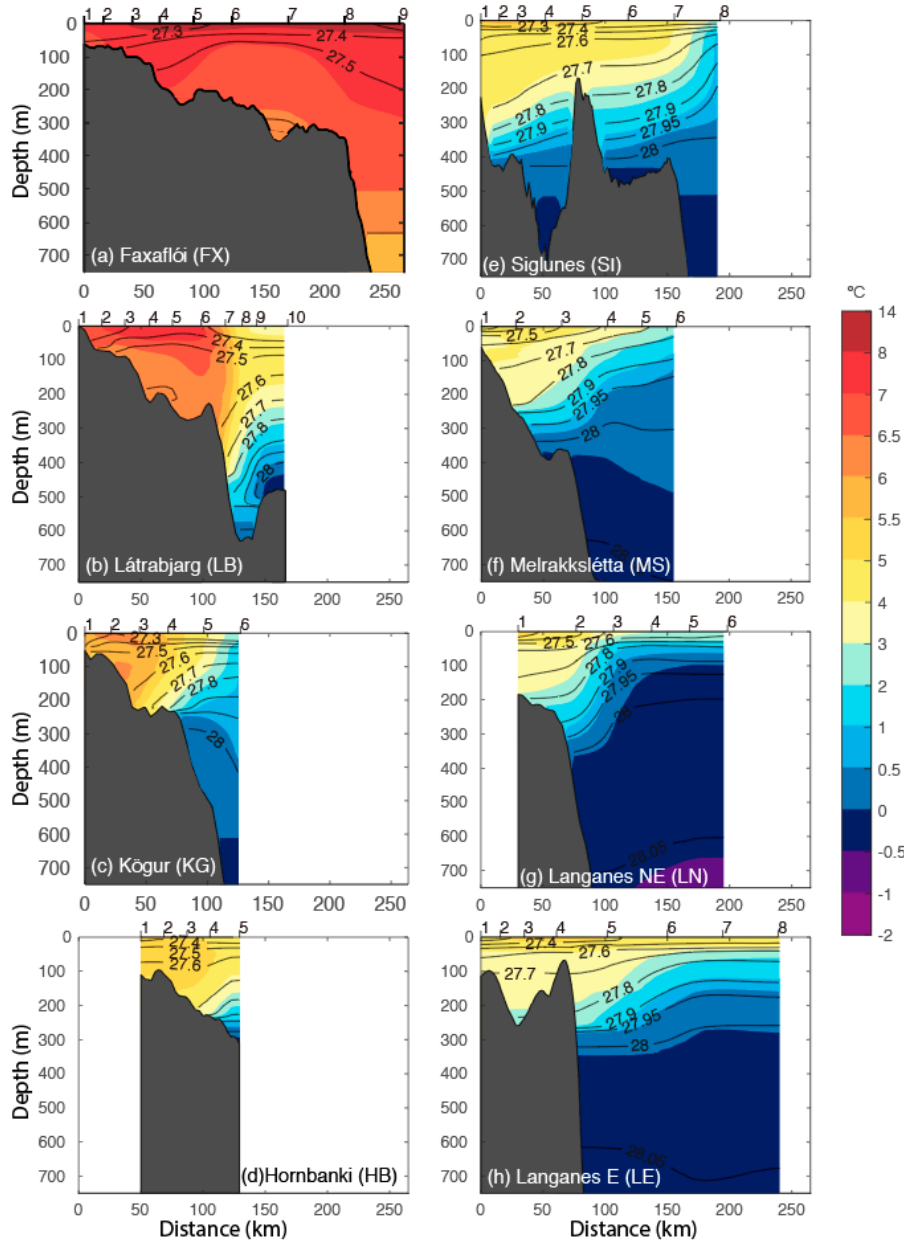
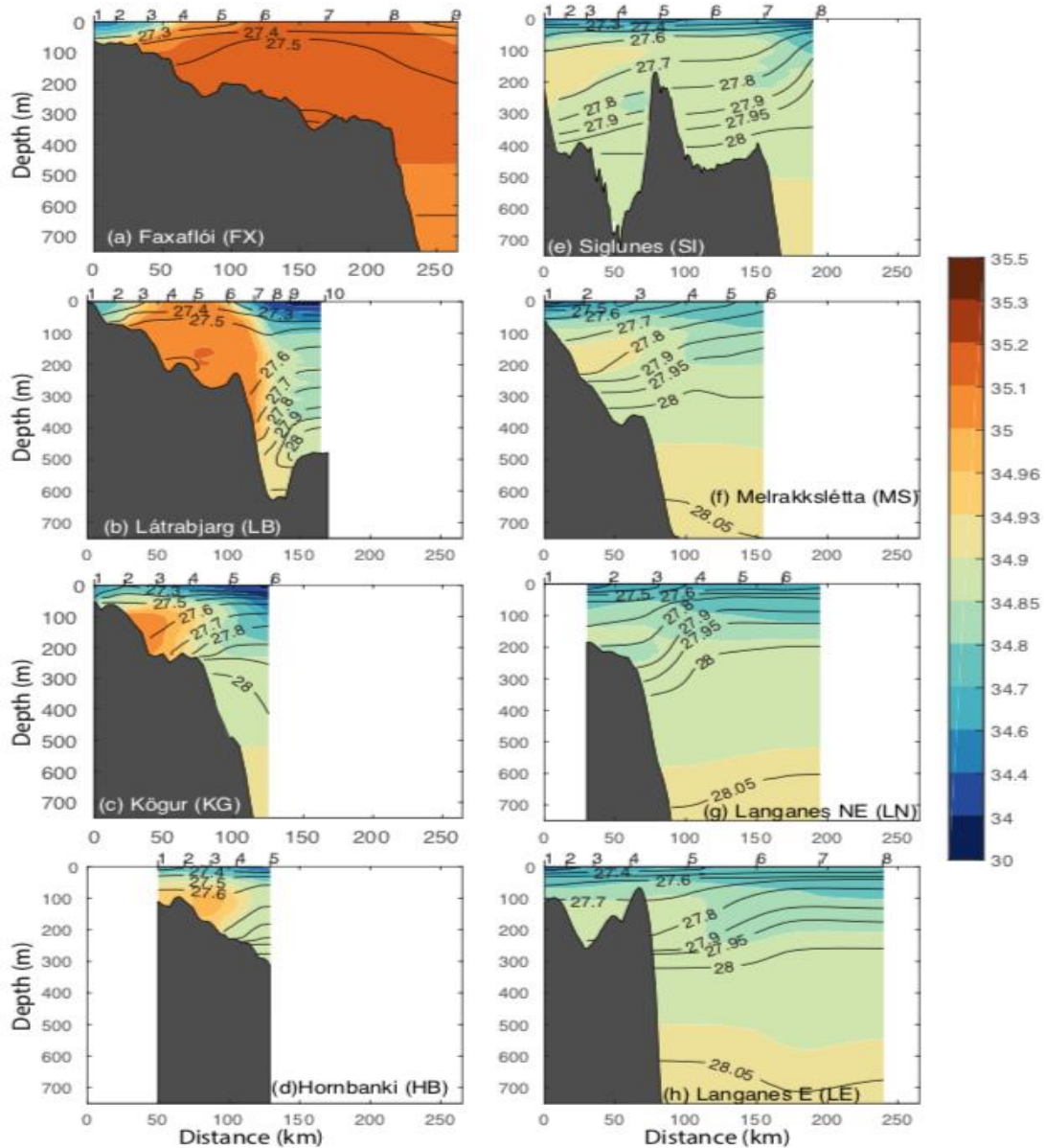


**Figure 3:** Mean vertical sections of potential temperature (color, °C) overlain by potential density (contours,  $\text{kg m}^{-3}$ ) for the different transects. Station locations and numbers are indicated along the top axis. The bottom topography is from the Smith and Sandwell Global Topography (Smith & Sandwell, 1997). (a) FX, (b) LB, (c) KG, (d) HB, (e) SI, (f) MS, (g) LNE, and (h) LE.

311



312

313 **Figure 4:** Same as Figure 3 except for salinity.

314

315

316

317

318

319

320

321

322

As explained above in Section 2.3, absolute geostrophic velocities were calculated at the 6 transects where the altimetry data were deemed accurate enough to be used for referencing the thermal wind shear. These mean vertical sections are shown in Fig. 5. At each transect we visually defined the location of the relevant currents: the Irminger Current, NIIC, EIC, and merged NIIC-EIC. At FX there are two branches of the Irminger Current; the inner branch corresponds to the positive flow from the coast to 140 km, and the outer branch corresponds to the positive flow seaward of 225 km (the outer branch was not completely sampled by the transect). At LB, the NIIC is the positive flow beyond 105 km from the coast. At KG and HB, the NIIC corresponds to all the positive flow (the HB transect did not bracket the entire current).

At SI, both the NIIC and EIC are present as separate cores (this is addressed further below). The former is defined as the positive flow from station 2 to 100 km, and the latter is taken to be the positive flow from 100 km to the end of the section (the section did not capture the entire EIC). At LE, the NIIC and EIC are merged, and the combined current is taken to be the positive flow from 0–175 km. Although there are no absolute geostrophic velocity data for the MS and LNE transects, the relative geostrophic velocity sections at these two locations indicate that the NIIC and EIC are merged here as well, i.e. there is a single well-defined relative geostrophic velocity core at each location (see Figs. 6 and 7).

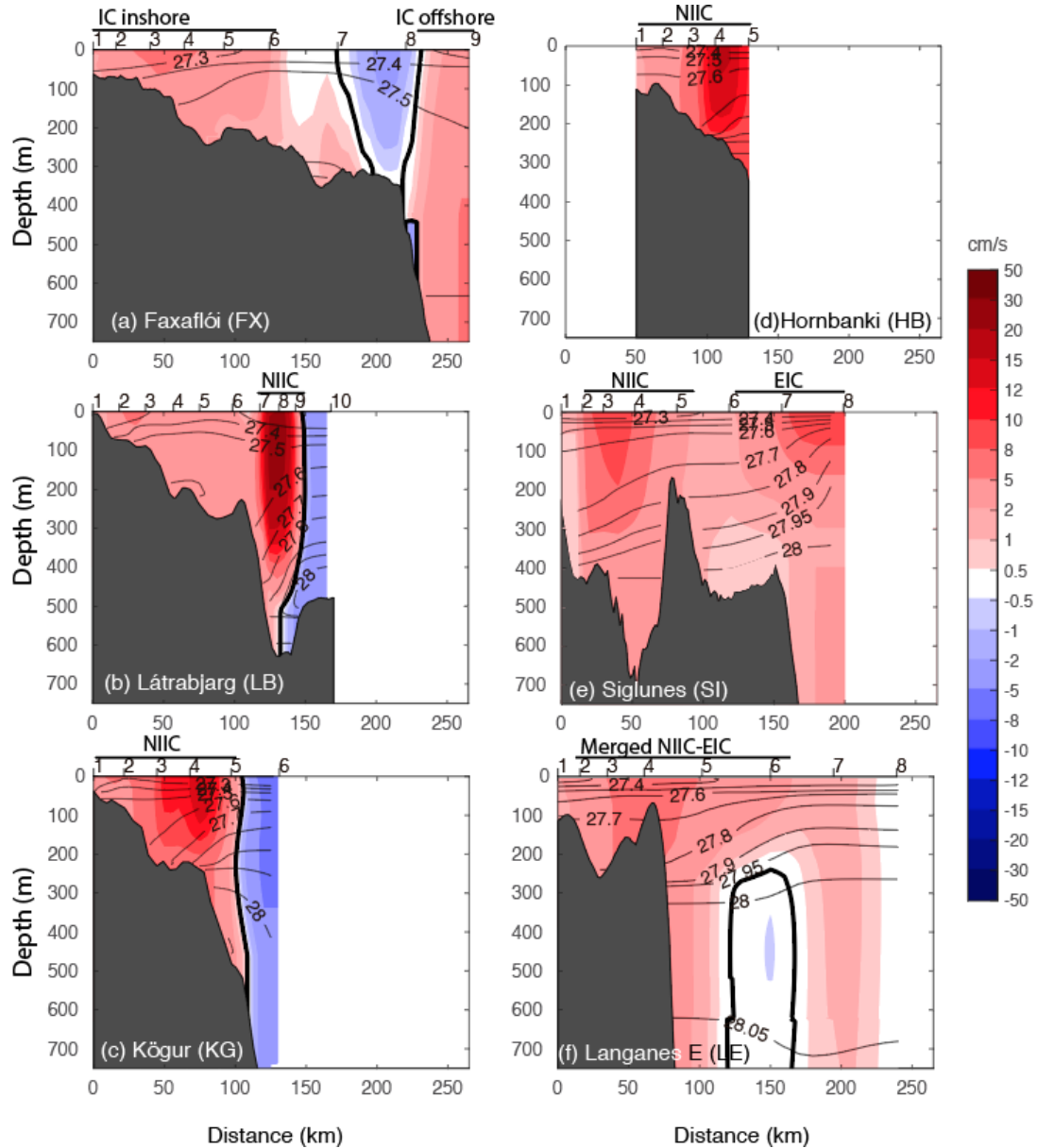


**Figure 5:** Same as Figure 3 except for the 6 transects with absolute geostrophic velocity ( $\text{cm s}^{-1}$ ). (a) FX, (b) LB, (c) KG, (d) HB, (e) SI, and (f) LE. Positive velocities (red) are clockwise currents around Iceland, and negative velocities are counter-clockwise currents. The thick black line is the zero-velocity contour. The names and locations of the currents are indicted at the top of each panel.

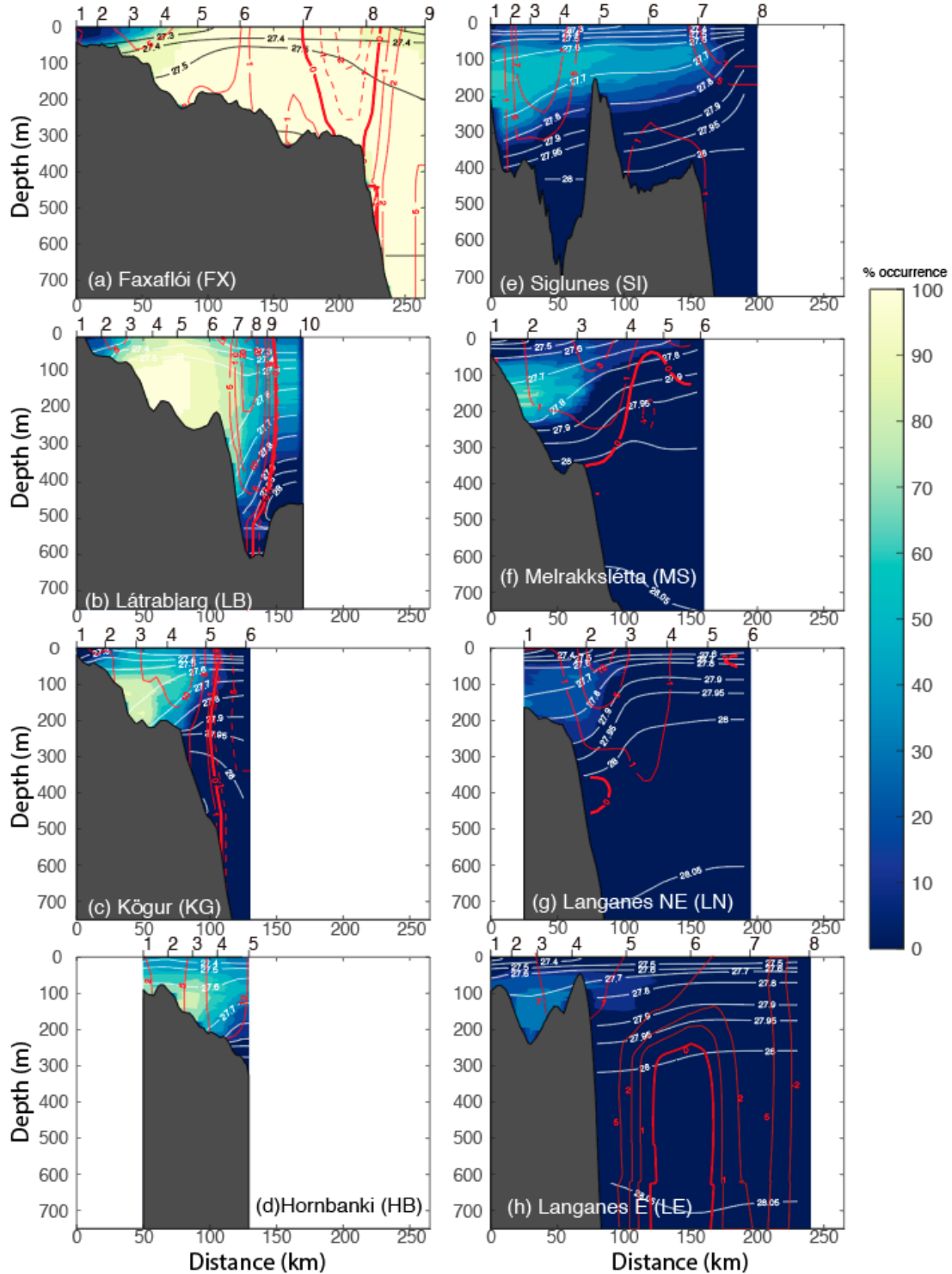


**Figure 6:** Vertical sections of percent occurrence of AW (color, %) at each transect overlain by potential density (black and white contours,  $\text{kg m}^{-3}$ ). The red contours ( $\text{cm s}^{-1}$ ) are the mean absolute geostrophic velocities from the 6 transects in Fig. 5, while for transects MS and LN they are the relative geostrophic velocities referenced to the bottom. Positive velocities (solid red contours) are clockwise currents around Iceland, and negative velocities (dashed red contours) are counter-clockwise currents.



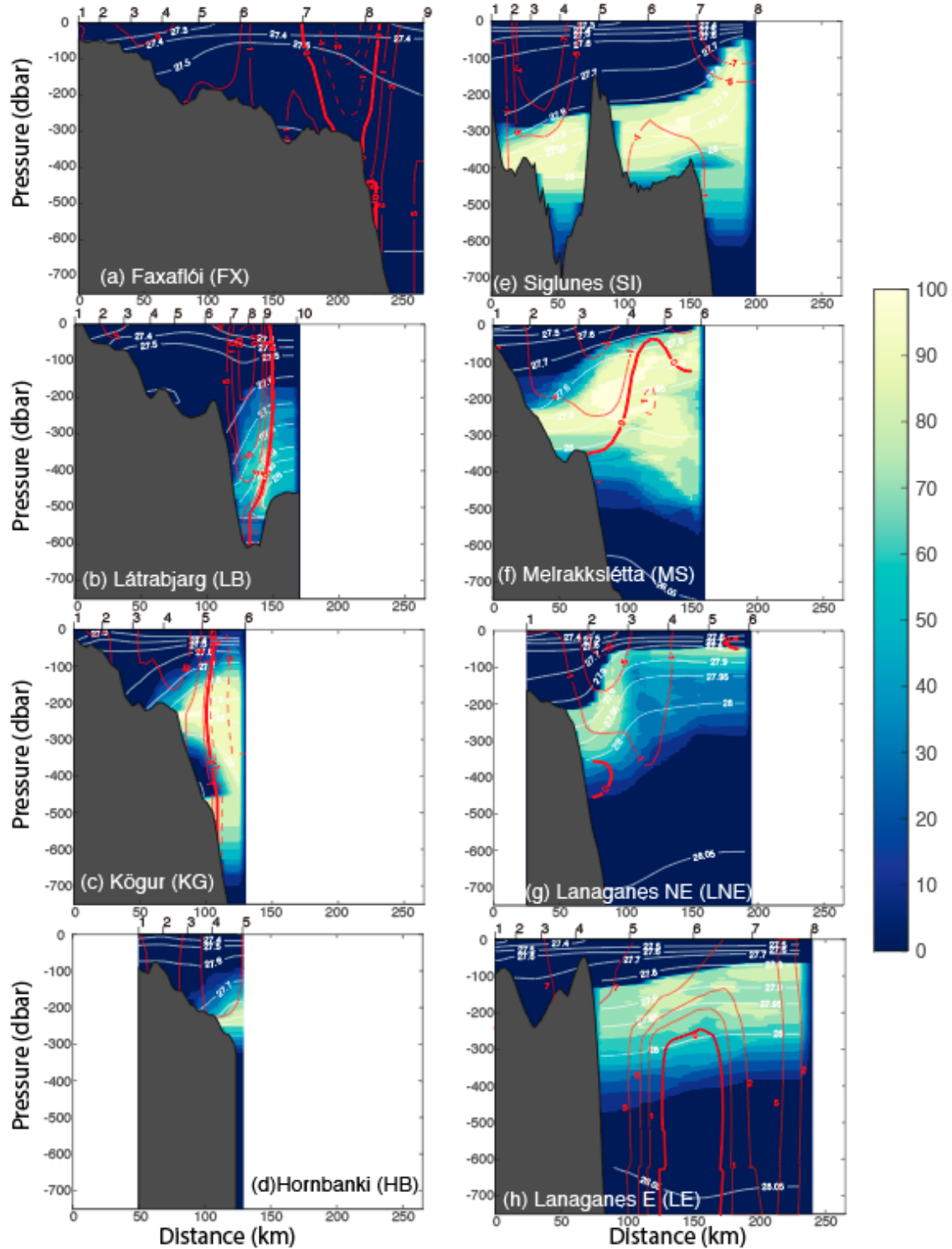


**Figure 7:** Same as in Fig. 6 except for percent occurrence of AtOW.

The two water masses most relevant to the currents being addressed in this study are the AW and AtOW. To quantify their presence, and how this changes going around Iceland, we did the following calculation. Using the definitions in Table 2 we identified the grid points corresponding to these water masses for every occupation of each transect. We then tabulated

this information and constructed vertical sections of the percent occurrence of the two water types (Figs. 6 and 7). We note that this is different from the end-member approach used by Jónsson & Valdimarsson (2012b) and Pickart et al. (2017) where they computed the percentage of pure AW in the NIIC. In our case we are simply tabulating the amount of water within the given T/S class.

Not surprisingly, nearly the entire FX section corresponds to 100% occurrence of AW, except for the stations on the very inner shelf where the AW is diluted by freshwater runoff (Fig. 6). In Denmark Strait the area of high occurrence shrinks considerably, but still reaches 100% on the mid shelf on the LB line. Within the NIIC at this transect, the AW occurrence varies from high values on the inshore side of the current (~80%) to low values on the offshore side (~40%). This is to be expected because the current is supported by the hydrographic front dividing the AW and SW, and mixing dilutes the two water masses. Over the next three sections (KG, HB, SI) the AW occurrence continues to decrease, although the NIIC is still characterized by presences of 40% or more. However, the outer core at SI is nearly void of AW, which supports the notion that this is the EIC. Farther to the east, where the NIIC and EIC are merged, the seaward side of the combined flow has essentially no AW occurrence, while the percentages on the inshore side of the current become considerably smaller than in Denmark Strait. Overall, the percent occurrence of AW drops from 100% near Denmark Strait to less than 25% northeast of Iceland.

The percent occurrence of AtOW tells a different story (Fig. 7). South of Denmark Strait at FX there is no presence of this water mass (as shown above, it is 100% AW except for near the coast). At the strait AtOW is present (up to 50%) in the deeper portion of the NIIC, likely introduced to the current via mixing with the southward flowing East Greenland Current. Over the next three sections (KG, HB, SI) AtOW is still confined to the lower reaches of the NIIC, but the percent occurrence increases. By contrast, the EIC at the SI line has a higher AtOW percentage throughout the current, and from that point onward the percent occurrence on the seaward side of the merged NIIC-EIC exceeds 70%. This is consistent with the notion that the EIC advects AtOW to the region north of Iceland, and that the resulting merged flow carries both water masses side by side. However, the percent occurrence of AtOW is much higher in the merged flow than that of AW (compare Fig. 6f,g,h to Fig. 7f,g,h). Notably, where the two currents first merge at the MS line, there is no AW on the seaward side of the current and no AtOW on the shoreward side, but by the next section the AtOW is prevalent across the entire merged current.

Volume transports were computed using the absolute geostrophic velocity sections. We limited the depth range to 650 m for the NIIC, which is the sill depth of Denmark Strait, and to 700m for the EIC and merged flow. The mean values for the six transects are shown in Table 3. The mean transport of the inshore branch of the Irminger Current at the FX line is  $0.80 \pm 0.04$  Sv (where the uncertainty is the standard error which represents the statistical uncertainty; Table 3). At section LB the NIIC transport is  $2.24 \pm 0.23$  Sv, which implies that some part of the offshore branch of the Irminger Current at FX also progresses through Denmark Strait to contribute to the NIIC, while the remaining part recirculates within the Irminger Sea (Fig. 1).

At the next section to the north, KG, the mean transport is  $1.16 \pm 0.11$  Sv, which is less than the transport of  $1.71 \pm 0.22$  Sv estimated by Pickart et al., (2017) (who used only 7 occupations of the transect). This reduction in transport from LB to KG is consistent with the

fact that there is AW present on the Greenland side of Denmark Strait at the LB line (Mastropole et al., 2017), which implies that some of the NIIC recirculates immediately north of the strait. At the HB and SI lines the mean NIIC transport estimates are  $1.37 \pm 0.05$  Sv and  $1.43 \pm 0.11$  Sv, respectively. As noted above, the EIC is present offshore of the NIIC at the SI line, and its transport is  $1.16 \pm 0.08$  Sv, although this is an underestimate since the transect does not extend far enough seaward to fully sample the current. Farther to the east the two currents merge, and at LE the mean transport of the combined flow is  $3.42 \pm 0.25$  Sv. Assuming that the mean EIC transport measured at the SI line is roughly half the true value (implied by Fig. 5e), this would suggest a combined NIIC+EIC transport of 3.75 Sv, which is close to the measured value at LE.

**Table 3:** NIIC, EIC, and NIIC-EIC merged flow mean absolute geostrophic transports (Sv), including standard errors.

Occupation	Absolute geostrophic transport
FX NIIC	$0.80 \pm 0.04$
LB NIIC	$2.24 \pm 0.23$
KG NIIC	$1.16 \pm 0.11$
HB NIIC	$1.37 \pm 0.05$
SI NIIC	$1.43 \pm 0.11$
SI EIC	$1.16 \pm 0.08$
SI merged	$2.59 \pm 0.15$
LE merged	$3.42 \pm 0.25$

Overall, our transport estimates provide a sensible accounting of the currents encircling Iceland: The inshore branch of the Irminger Current, together with part of the offshore branch, flow through Denmark Strait to form the NIIC. North of the strait, part of the NIIC recirculates back to the south on the western side of the strait. The remaining flow continues eastward and is joined by the eastward-flowing EIC north of Iceland. These two currents, originally flowing side by side as separate cores, subsequently merge and continue to the northeast part of Iceland as a single core – consistent with the hydrographic measurements. Interestingly, we see no evidence of detrainment of the NIIC as it flows around Iceland, which is implied by the drifter observations of Valdimarsson & Malverg (1999) and the model results of Våge et al. (2011). However, the AW occurrence drops by 75% from Denmark Strait to northeast Iceland.

#### 4 Vorticity

We now explore the potential vorticity structure of the NIIC to shed light on its stability characteristics. The Ertel potential vorticity ( $\Pi$ ) can be expressed as:

$$\Pi = \frac{-f}{\rho_0} \frac{\partial \sigma_\theta}{\partial z} + \frac{1}{\rho_0} \frac{\partial u}{\partial y} \frac{\partial \sigma_\theta}{\partial z} - \frac{g}{\rho_0^2 f} \left( \frac{\partial \sigma_\theta}{\partial y} \right)^2, \quad (1)$$

where  $f$  is the Coriolis parameter (which is  $1.33 \times 10^{-4} \text{ s}^{-1}$  averaged over all station locations),  $g$  is the gravitational acceleration,  $\rho_0$  is the reference density ( $1028 \text{ kg m}^{-3}$ ),  $z$  is the depth,  $\sigma_\theta$  is the potential density, and  $u$  is the absolute geostrophic velocity. The Ertel potential vorticity has three components: the stretching vorticity, relative vorticity, and tilting vorticity (Hall, 1994), of which the stretching vorticity typically dominates for large-scale currents (McCartney & Talley, 1982; Pickart et al., 2005).



We calculated the different terms of  $\Pi$  for all occupations of the transects where there were absolute geostrophic velocities. For the mean sections, the lateral gradients of the NIIC velocity (Fig. 8a,b), as well as the merged NIIC-EIC (Fig. 8c), correspond to very small values of relative vorticity. When normalized by the stretching vorticity, which is a measure of the Rossby number, the maximum values are between 0.01–0.02. Instantaneously, however, the values can be much larger. For each occupation we determined the maximum cyclonic and minimum anti-cyclonic relative vorticity for the NIIC progressing from Denmark Strait to northeast Iceland, including the merged NIIC-EIC at LE (Fig. 9). The largest spread in Rossby number occurs at the LB line, with values at times near 0.4, indicating that the current can be non-linear as it flows through Denmark Strait. Proceeding downstream, the Rossby numbers generally decrease with the smallest values at LE, the eastern-most section where the NIIC and EIC are merged. These results suggest that the NIIC is not likely to be subject to barotropic instability.

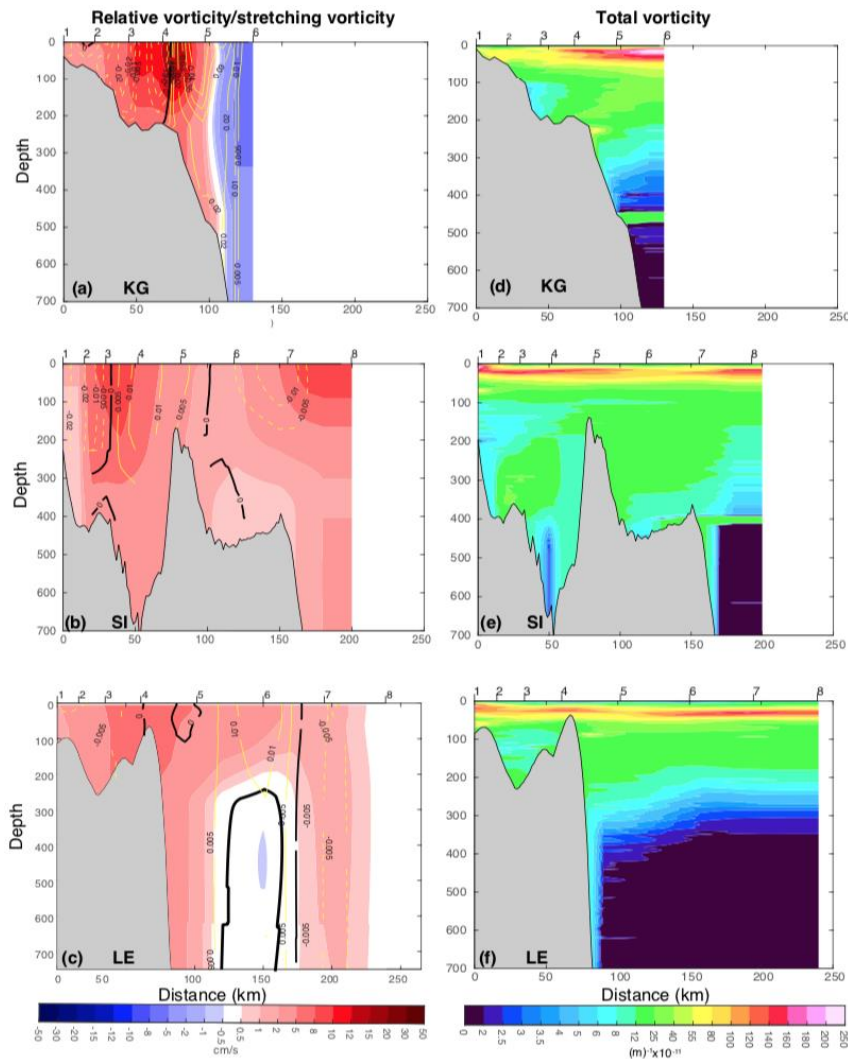


**Figure 8:** (left-hand column) Mean vertical sections of absolute geostrophic velocity from Fig. 5 (color) overlain by the mean values of relative vorticity divided by stretching vorticity (yellow contours; the black contour is the zero value). (right-hand column) Mean vertical sections of Ertel potential vorticity (color). Three transects shown are: KG (panels a and d) and SI (panels b and e) before the NIIC and EIC have merged, and LE (panels c and f) after the currents have merged.

Not surprisingly, the potential vorticity is dominated by the stretching vorticity term. Vertical sections of  $\Pi$  are shown in Fig. 8d-f for three transects: KG and SI (NIIC), and LE (merged NIIC-EIC). In all three cases the lateral gradient of  $\Pi$  changes sign with depth. For example, at the KG line  $\Pi$  increases progressing offshore in the upper 200 m, whereas it decreases going offshore in the depth range 200-400 m, which is the deepest portion of the current. Such a change in sign in the gradient of  $\Pi$  satisfies the necessary condition for baroclinic instability. This suggests that the NIIC is apt to meander and form eddies, which could explain why surface drifters are readily expelled from the current Valdimarsson & Malmberg (1999). Baroclinic instability does not by itself, however, imply a loss of volume transport (Spall et al., 2008), which is consistent with the transport results presented above.

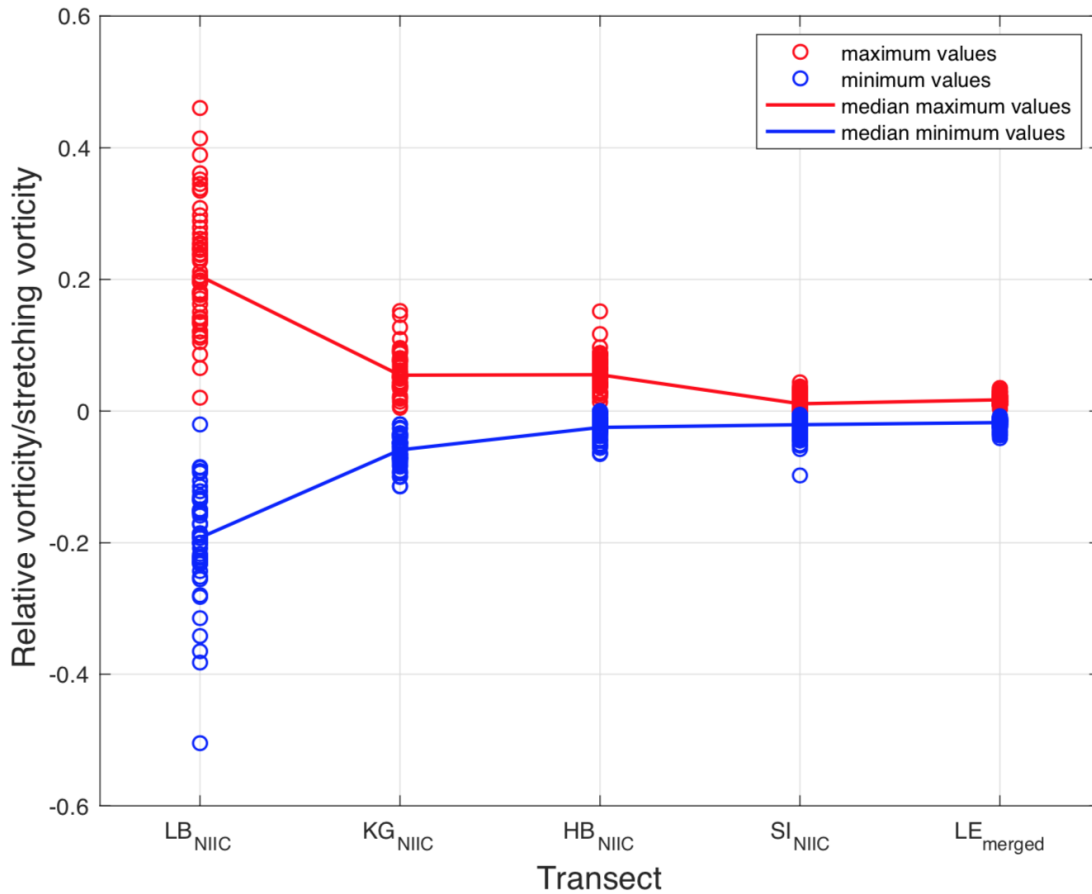


**Figure 9:** Maximum and minimum values of relative vorticity divided by stretching vorticity in the NIIC (merged NIIC-EIC) for all occupations of transects LB, KG, HB, SI, (LE). Red (blue) circles are cyclonic (anti-cyclonic) vorticity. The solid lines represent the median values.

## 5 Alongstream seasonal variability

Using the water mass definitions in Table 2 and the criteria for delimiting the currents described in section 3, we now quantify the seasonal modification of the water advected by the flow encircling Iceland. This is done by considering the average properties of the current as well as isolating the component water masses within the current. For the transects where there are no absolute geostrophic velocities (MS and LNE) we used the relative geostrophic velocity sections (referenced to the bottom) to define the location of the merged NIIC-EIC. Fig. 2b documents the

465 alongstream change in properties of the flow as it transitions from the Irminger Current to the  
 466 NIIC to the merged NIIC-EIC during each season (the outer EIC core at SI is not considered  
 467 here). During winter the current is principally comprised of AW at FX and LB. At the next three  
 468 sections (KG, LB, SI) the water is near the boundaries of AW, AtOW, and SW. Farther to the  
 469 east the merged NIIC-EIC is mostly cold AtOW (close to the boundary of ArOW). Wintertime  
 470 cooling may result in the formation of intermediate water ( $\sigma_\theta > 27.70 \text{ kg m}^{-3}$ ) on the Iceland  
 471 shelf (Våge et al., 2015). This locally transformed AW would have hydrographic properties  
 472 within the AtOW class (Fig. 2a). In spring the current is predominantly AW from FX all the way  
 473 to HB; beyond this the current has a water mass composition similar to that in winter. In summer  
 474 and fall, only the flow at FX is comprised mostly of AW. From Denmark Strait to SI the  
 475 dominant water mass advected by the current is SW. Once the NIIC and EIC merge at MS,  
 476 however, the current again has a water mass composition similar to the other seasons. Thus, there  
 477 is considerably more seasonal and alongstream variability in the properties of the flow prior to  
 478 the merging of the NIIC and EIC.

479 The evolution of the AW signature within the flow as it progresses around Iceland is  
 480 documented in Fig. 2c. This demonstrates that some amount of AW is present at all of the  
 481 transects in every season (there are no winter data at MS). The signal generally gets colder and  
 482 fresher progressing around Iceland, though the biggest alongstream change takes place during  
 483 summer and fall. The AW entering the Iceland Sea through Denmark Strait at LB is warmest in  
 484 summer and fall, and the AW appearing at the farthest east sections (LNE and LE) is coldest in  
 485 spring. Consistent with this, Macrander et al. (2014) suggested that at LNE the AW is warmer in  
 486 summer and fall. Figure 2d shows the AtOW present in the NIIC at LB, KG, HB and SI, and in  
 487 the merged flow at MS, LNE, and LE (this water mass is not present south of Denmark Strait,  
 488 Fig. 7). AtOW does not seem to have a clear seasonality. However, there are some differences  
 489 between transects. Most notably, AtOW at LB and KG is fresher and cooler than at HB and SI,  
 490 probably due to the fact that, progressing away from Denmark Strait, the water continues to mix  
 491 with the warmer and saltier water of the NIIC or a larger proportion of the water in the AtOW  
 492 class is locally formed.

493 Lateral maps were constructed for each season to help shed light on the evolution of  
 494 water properties around Iceland. Specifically, we averaged the potential temperature and salinity  
 495 over the upper 300 m using the interpolated and gridded CTD data to highlight the NIIC layer  
 496 (Fig. 10). The temperature maps show that waters with  $\theta \geq 3^\circ\text{C}$  (in the mid-temperature range of  
 497 AW) occupy the Iceland shelf in summer and fall (Figs. 10c,d), while in winter and spring only  
 498 the west and northwest Iceland shelf is occupied with waters that warm (Figs. 10a,b). The fate of  
 499 the AW is more readily assessed using the salinity maps. In all four seasons relatively high  
 500 values of salinity ( $>35.2$ ) extend to the LB line, but not to HB (although in spring the salinity is a  
 501 bit higher there than the other seasons). Over the northern shelf the salinities are highest in  
 502 summer (Fig. 10g) and lowest in the fall (Fig. 10h). During winter the values are relatively  
 503 uniform east of HB (Fig. 10e), which is likely a reflection of convective overturning.

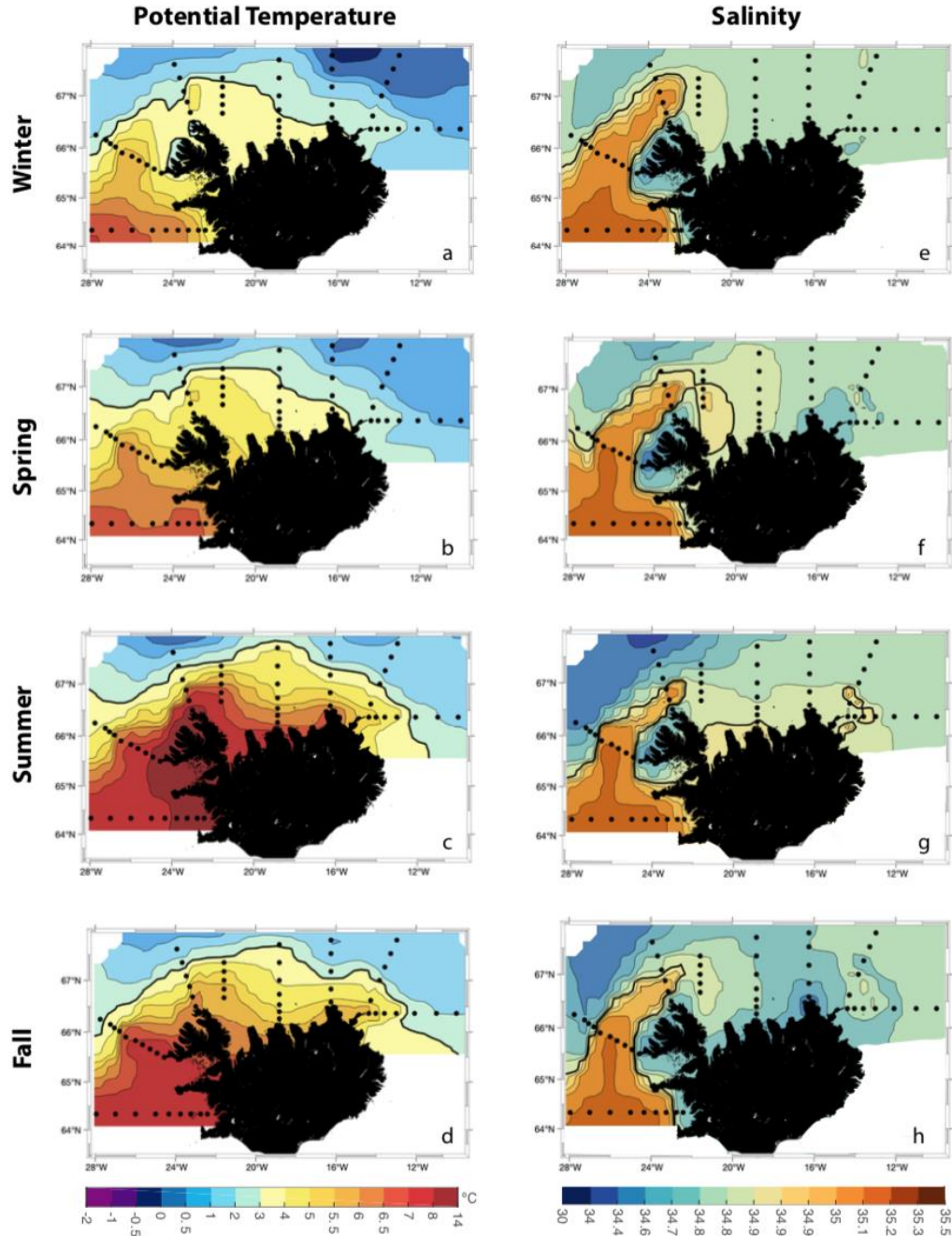


**Figure 10:** Lateral maps of mean potential temperature ( $^{\circ}\text{C}$ ) and salinity per season, averaged from the surface to 300 m depth. The thick black line in the temperature and salinity maps represents the approximate boundary between the AW and the PW.

## 6 Interannual variability

We now consider the year-to-year changes in the properties and transports of the currents encircling Iceland. To simplify the analysis, we divided the domain into two regions: an upstream region in which we average the LB, KG, HB, and SI transects (inner velocity core only for the SI transect), and a downstream region which corresponds to the LE section (this is the

only downstream section with absolute geostrophic velocity). Prior to computing the annual averages, we subtracted the monthly mean from each transect to remove the effect of seasonality. In the upstream region we considered the interannual signal of the NIIC and that of the AW within the NIIC, and for the downstream region we considered the merged NIIC-EIC and the AtOW within the merged flow. We show the yearly values as well as the 12-month low pass, and also include the regression lines (the regression lines are shown only if they correspond to a confidence level exceeding 0.9). The results are displayed in Fig. 11 for temperature, Fig. 12 for salinity, and Fig. 13 for volume transport. Table 4 documents the net change in these quantities from 1993 to 2017 based on the regression lines.

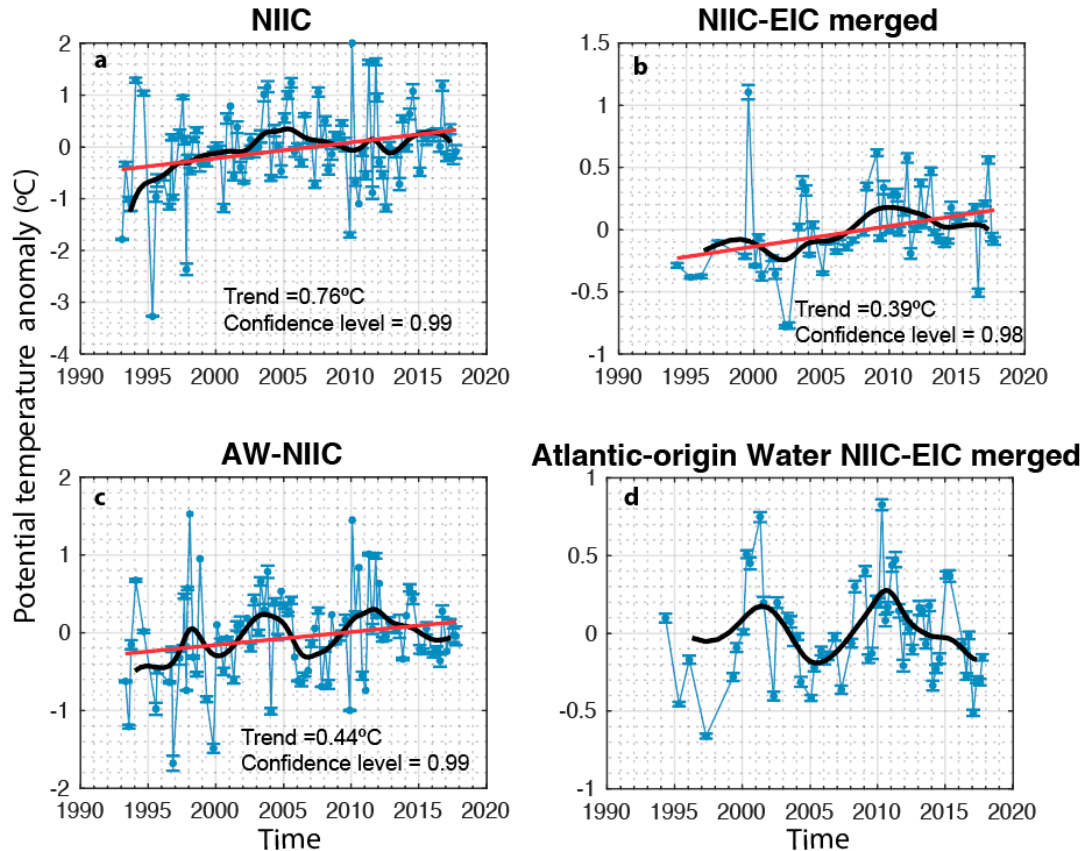


**Figure 11:** Time series of annual mean potential temperature (blue circles, °C) where the seasonal signal was removed for each occupation prior to averaging. The standard errors are included. The thick black line is the 12-month low pass. The red line is the linear regression, which is shown only for those cases where the confidence level exceeds 0.9. (a) The NIIC from LB to SI. (b) The NIIC-EIC merged flow at LE. (c) The AW within the NIIC. (d) The AtOW within the NIIC-EIC merged flow.

Over the 25-year study period, the NIIC has become warmer, saltier, and its transport has increased (Figs. 11a, 12a, 13a; Table 4). Interestingly, the AW within the NIIC has undergone less net change in temperature and salinity (Figs. 11c, 12c). The explanation is that the SW portion of the NIIC has become warmer and saltier over this time period (not shown). By contrast, the increase in volume transport of the NIIC is explainable by the change in transport of the AW portion of the flow (Figs. 13a,c). The merged NIIC-EIC has also become warmer and saltier over the 25-year time period, but its transport has not significantly changed (Figs. 11b,



12b, 13b; Table 4). The increase in salinity is largely due to salinification of the AtOW (Fig. 12d), but the temperature increase is mostly due to the SW (not shown).

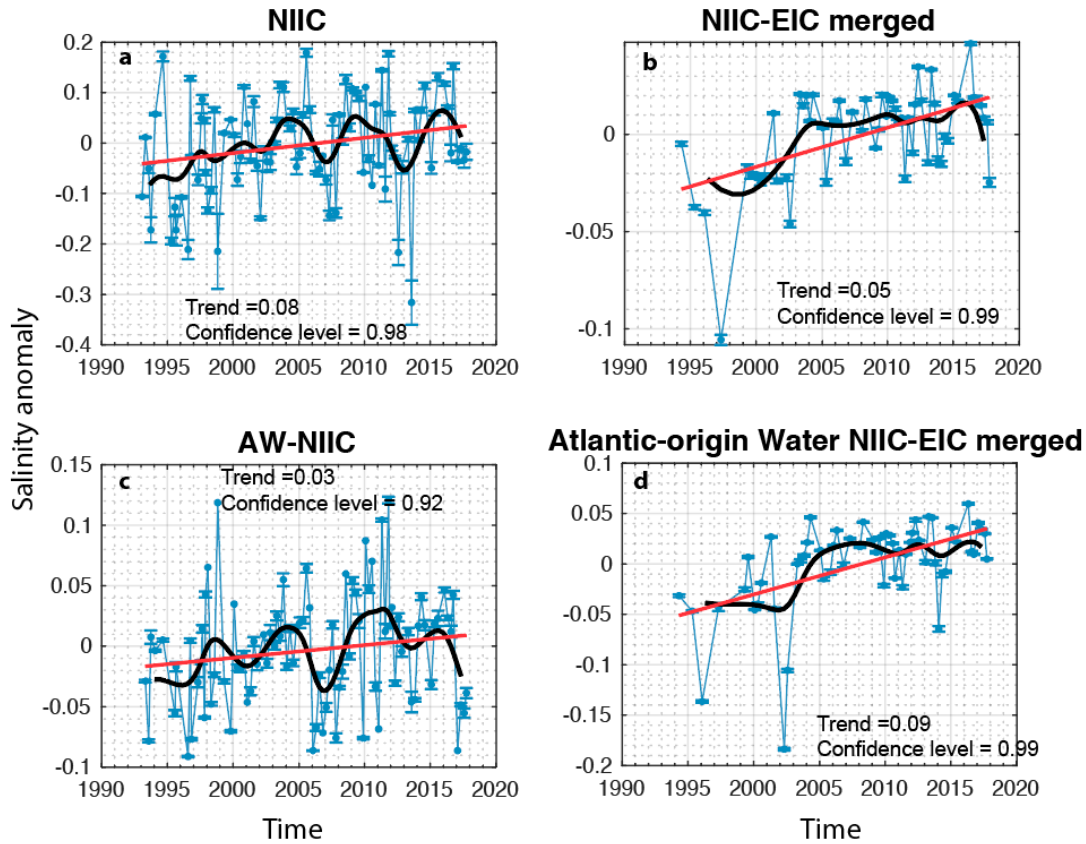


**Figure 12:** Same as Figure 11 except for salinity.

**Table 4:** Net change in potential temperature ( $\theta$ ), salinity ( $S$ ), and volume transport from 1993 to 2017. Entries with a dash had no significant change.

	$\Delta\theta$ ( $^{\circ}\text{C}$ )	$\Delta S$	$\Delta\text{Transport}$ ( $\text{Sv}$ )
NIIC	0.76	0.08	0.68
NIIC-EIC	0.39	0.05	—
AW	0.44	0.03	0.70
AtOW	—	0.09	—

In addition to the net changes over the 25-year period, the 12-month Low-pass curves reveal that there has been significant interannual variability in most of the variables. Notably, while there is only a modest long-term trend in the properties of the AW advected by the currents encircling Iceland, the temperature and salinity of the water vary in phase with each other on roughly a 5-year period with a relatively large amplitude (Figs. 11c, 12c). Furthermore, the warm/salty periods are associated with enhanced transport of the NIIC (Fig. 13a) as well as increased transport of the AW within the NIIC (Figs. 13c).

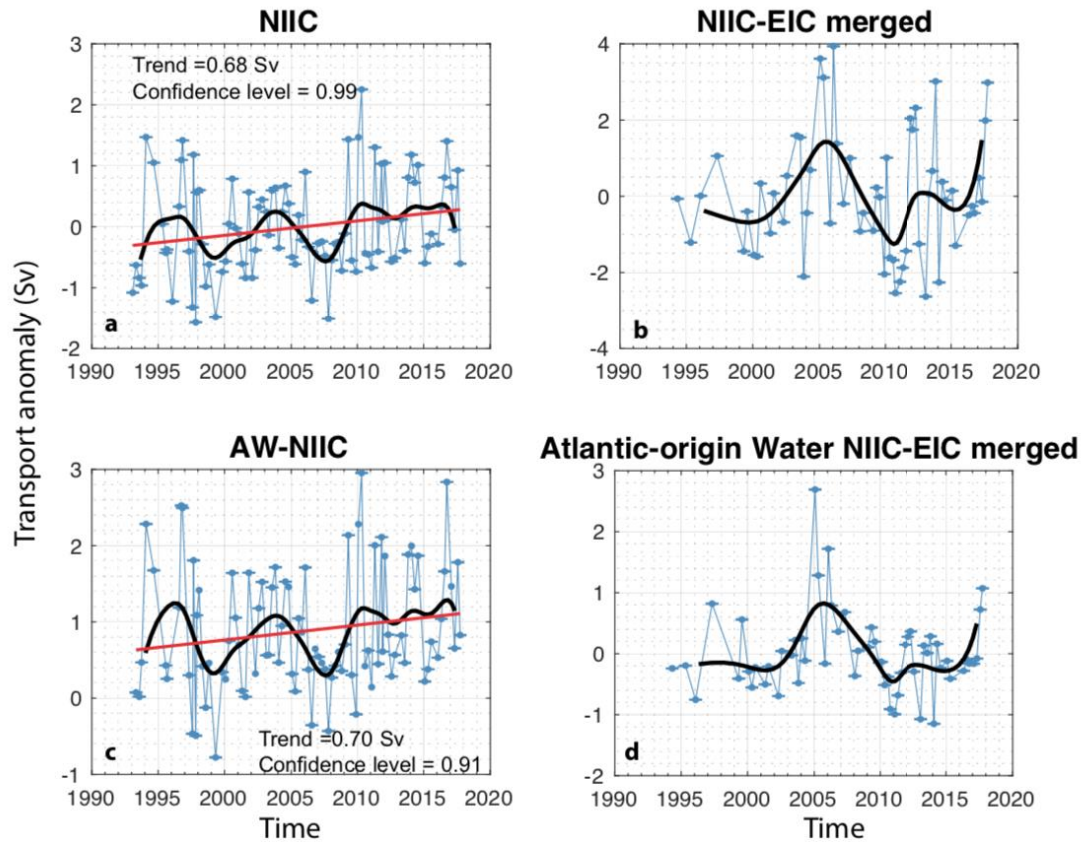


**Figure 13:** Same as Figure 11 except for volume transport (Sv).

To further explore the nature of the interannual changes, we did a correlation analysis between the observed variability in Figs. 11-13 and the climatic indices of the North Atlantic Oscillation (NAO), the Atlantic Multidecadal oscillation (AMO), and the Greenland Blocking Index (GBI). A few clear statistically significant connections emerged. The GBI is defined as the mean 500-hPa height over the Greenland area 60–80°N, 20–80°W. Its positive state, associated with blocking events, corresponds to enhanced anticyclonic atmospheric circulation over Greenland (Kwon et al., 2020). Our results indicate that the positive (negative) state of the GBI leads to lower (higher) transports of the NIIC and merged flow, with a phase lag of 0 years. This is to be expected in that the enhanced northerly winds in the positive state oppose the northward flow through Denmark Strait.

The correlation analysis with the NAO index indicates that both the NIIC and NIIC-EIC merged flow weaken, and the temperature of the AW within the NIIC decreases, in the NAO+ phase, with a time lag of 1-2 years. This is consistent with the results of Flatau et al. (2003). At the same time, during the NAO+ phase the precipitation in the western subpolar North Atlantic increases (Frankignoul et al., 2009), which suggests that the salinity of the AW entering the Iceland Sea would decrease. Indeed, we find such a relationship in our data with a 0-year time lag. With regard to the AMO, the most notable connection involves the AW within the NIIC and NIIC-EIC merged flow. Specifically, in positive AMO phases, which correspond to warm sea surface temperatures in the North Atlantic, the temperature and salinity of the AW increase in concert with the highest values of the index.

## 7 Summary

In this study, we have used 25 years of hydrographic data to analyze the spatial, seasonal, and interannual variability of the currents and water masses flowing northward and eastward on Iceland's slope and shelf. The velocity data indicate that some portion of the NIIC recirculates just north of Denmark Strait, while the remaining portion is joined by the EIC in the vicinity of the Kolbeinsey Ridge north of Iceland. The currents initially flow side by side, but then merge into a single current that extends to the eastern-most section considered in this study. Notably, there seems to be no loss of transport of the NIIC, EIC, and merged NIIC-EIC after the initial recirculation north of Denmark Strait, which is counter to previous results suggesting that the NIIC weakens and detrains as it flows around Iceland.

The main water mass of the NIIC is the warm and salty AW transported to Denmark Strait by the Irminger Current, while the predominant water mass of the EIC is the cooler and fresher AtOW which stems from the East Greenland slope. The percentage of AW in the NIIC and merged flow decreases steadily as it flows around Iceland, with an overall drop from 100% near Denmark Strait to less than 25% northeast of Iceland. The percentage of AtOW in the EIC and merged flow does not decrease as much, and the signature of this water mass spreads throughout the merged current. By comparison, the AW signature in the merged flow remains on the seaward side of the current.

A vorticity analysis of the NIIC and merged current demonstrated that, unsurprisingly, the total Ertel potential vorticity ( $\Pi$ ) is dominated by the stretching term. The values of cyclonic and anti-cyclonic relative vorticity on the two sides of the current are comparable, and as the current progresses around Iceland their magnitudes decrease. The only transect that displays somewhat large Rossby numbers is the LB line at Denmark Strait, where individual crossings have values as large as 0.3–0.4. The vertical sections of  $\Pi$  show that the cross-stream gradient changes sign with depth, indicating that both the NIIC and merged flow are baroclinically unstable. This is consistent with the documented exchange of water between the current and the interior Iceland Sea.

A seasonal accounting of the water masses within the currents indicates that only in springtime is the NIIC dominated by AW north of Denmark Strait. In the remaining seasons other water masses contribute significantly, and in summer and fall the dominant water mass is SW. Isolating the AW signal demonstrates that it generally gets colder and fresher progressing around Iceland. The biggest alongstream change takes place during summer and fall, when the AW flowing through Denmark Strait is warmest. The AW appearing at the farthest east sections is coldest in spring. The AtOW does not have a clear seasonality. Overall, there is considerably more seasonal and alongstream variability in the properties of the flow prior to the merging of the NIIC and EIC.

Over the full 25-year period of data coverage, the NIIC has become warmer and saltier, and increased in transport. The same is not true, however, for the AW portion of the flow, which has undergone very little net change. This is due to the large influence of the SW on the flow. By contrast, the AW portion varies strongly on interannual timescales. During times when it is warmer and saltier its transport is larger, and vice versa. These changes occur on roughly a five-year period. A correlation analysis with known climate indices revealed several statistically significant relationships. Most notably, the transport of the NIIC and merged NIIC-EIC vary in phase with the GBI, which is to be expected based on the associated wind forcing in the vicinity



of Denmark Strait. The NAO also impacts these transports, but with a phase offset of 1-2 years. Finally, the temperature and salinity of the AW within the NIIC and NIIC-EIC merged flow vary in accordance with the AMO. Further work is required to elucidate more thoroughly the causes of some of these relationships.

## Acknowledgments, Samples, and Data

This research was supported by RIS-3, PO Feder Canarias through project BOUNDARY (ProID2017010083) and the SAGA project (CRTI2018-100844-B-C31) funded by the Ministerio de Ciencia, Innovación y Universidades of the Spanish Government. Additional support was provided by US National Science Foundation grants OCE-1756361 and OCE- 1558742. Additional support was provided from the Trond Mohn Foundation grant BFS2016REK01. This study was also supported by the Blue-Action project, which has received funding from the European Union's Horizon 2020 research and innovation programme under grant agreement No 727852. The ECMWF wind data were obtained from <https://www.ecmwf.int/>), and the altimetry data were obtained from the Aviso database <http://www.aviso.altimetry.fr/>. The hydrographic data can be downloaded from SeaDataNet (<https://www.seadatanet.org/>). This article is a publication of the Unida ma of the Universidad de Las Palmas de Gran Canaria, a R&D&i CSIC-associate unit. This work has been completed as part of MC-M work at IOCAG, in the doctoral program in Oceanography and Global Change. The lead author acknowledges the Agencia Canaria the Investigación, Innovación y Sociedad de la Información (ACIISI) grant program of “apoyo al personal investigador en formación” TESIS2017010023 , as well as MFRI for hosting a guest student to develop the study.

## References

- Behrens, E., Våge, K., Harden, B., Biastoch, A., & Böning, C. W. (2017). Composition and variability of the Denmark Strait Overflow Water in a high-resolution numerical model hindcast simulation. *Journal of Geophysical Research: Oceans*, 122(4), 2830–2846. <https://doi.org/10.1002/2016JC012158>
- Bersch, M. (1995). On the circulation of the northeastern North Atlantic. *Deep-Sea Research Part I*, 42(9), 1583–1607. [https://doi.org/10.1016/0967-0637\(95\)00071-D](https://doi.org/10.1016/0967-0637(95)00071-D)
- Blunden, J., & Arndt, D. S. (2016). State of the Climate in 2015. *Bulletin of the American Meteorological Society*, 97(8), Si-S275. <https://doi.org/10.1175/2016BAMSStateoftheClimate.1>
- Comas-Rodríguez, I., Hernández-Guerra, A., & McDonagh, E. L. (2010). Referencing geostrophic velocities using ADCP data Referencing geostrophic velocities using ADCP data. *Scientia Marina*, 74(2), 331–338. <https://doi.org/10.3989/scimar.2010.74n2331>
- Dee, D. P., Uppala, S. M., Simmons, A. J., Berrisford, P., Poli, P., Kobayashi, S., et al. (2011). The ERA-Interim reanalysis: Configuration and performance of the data assimilation system. *Quarterly Journal of the Royal Meteorological Society*, 137(656), 553–597. <https://doi.org/10.1002/qj.828>
- Ducet, N., Le Traon, P. Y., & Reverdin, G. (2000). Global high-resolution mapping of ocean circulation from TOPEX/Poseidon and ERS-1 and -2. *Journal of Geophysical Research: Oceans*, 105(C8), 19477–19498. <https://doi.org/10.1029/2000JC900063>

- 660 Egbert, G. D., & Erofeeva, S. Y. (2002). Efficient inverse modeling of barotropic ocean tides.  
661 *Journal of Atmospheric and Oceanic Technology*, 19(2), 183–204.  
662 [https://doi.org/10.1175/1520-0426\(2002\)019<0183:EIMOBO>2.0.CO;2](https://doi.org/10.1175/1520-0426(2002)019<0183:EIMOBO>2.0.CO;2)
- 663 Egbert, G. D., Bennett, A. F., & Foreman, M. G. G. (1994). TOPEX/POSEIDON tides estimated  
664 using a global inverse model. *Journal of Geophysical Research*, 99(C12), 24821.  
665 <https://doi.org/10.1029/94JC01894>
- 666 Enfield, D. B., Mestas-Núñez, A. M., & Trimble, P. J. (2001). The Atlantic Multidecadal  
667 Oscillation and its relation to rainfall and river flows in the continental U.S. *Geophysical*  
668 *Research Letters*, 28(10), 2077–2080. <https://doi.org/10.1029/2000GL012745>
- 669 Flatau, M. K., Talley, L., & Niiler, P. P. (2003). The North Atlantic Oscillation, surface current  
670 velocities, and SST changes in the subpolar North Atlantic. *Journal of Climate*, 16(14),  
671 2355–2369. <https://doi.org/10.1175/2787.1>
- 672 Frankignoul, C., Deshayes, J., & Curry, R. (2009). The role of salinity in the decadal variability  
673 of the North Atlantic meridional overturning circulation. *Climate Dynamics*, 33(6), 777–  
674 793. <https://doi.org/10.1007/s00382-008-0523-2>
- 675 Hall, M. M. (1994). Synthesizing the Gulf Stream Thermal Structure from XBT Data. *Journal of*  
676 *Physical Oceanography*, 24(11), 2278–2287. [https://doi.org/10.1175/1520-](https://doi.org/10.1175/1520-0485(1994)024<2278:STGSTS>2.0.CO;2)  
677 [0485\(1994\)024<2278:STGSTS>2.0.CO;2](https://doi.org/10.1175/1520-0485(1994)024<2278:STGSTS>2.0.CO;2)
- 678 Hamilton, L. C., Jónsson, S., Ögmundardóttir, H., & Belkin, I. M. (2004). Sea Changes Ashore :  
679 The Ocean and Iceland’s Herring Capital. *ARCTIC*, 57(4), 325–335.  
680 <https://doi.org/10.14430/arctic511>
- 681 Hanna, E., Jones, J. M., Cappelen, J., Mernild, S. H., Wood, L., Steffen, K., & Huybrechts, P.  
682 (2013). The influence of North Atlantic atmospheric and oceanic forcing effects on 1900–  
683 2010 Greenland summer climate and ice melt/runoff. *International Journal of Climatology*,  
684 33(4), 862–880. <https://doi.org/10.1002/joc.3475>
- 685 Hansen, B., & Østerhus, S. (2000). North Atlantic–Nordic Seas exchanges. *Progress in*  
686 *Oceanography*, 45(2), 109–208. [https://doi.org/10.1016/S0079-6611\(99\)00052-X](https://doi.org/10.1016/S0079-6611(99)00052-X)
- 687 Harden, B. E., Pickart, R. S., Valdimarsson, H., Våge, K., de Steur, L., Richards, C., et al.  
688 (2016). Upstream sources of the Denmark Strait Overflow: Observations from a high-  
689 resolution mooring array. *Deep Sea Research Part I: Oceanographic Research Papers*, 112,  
690 94–112. <https://doi.org/10.1016/j.dsr.2016.02.007>
- 691 Håvik, L., Pickart, R. S., Våge, K., Torres, D., Thurnherr, A. M., Beszczynska-Möller, A., et al.  
692 (2017). Evolution of the East Greenland Current from Fram Strait to Denmark Strait:  
693 Synoptic measurements from summer 2012. *Journal of Geophysical Research: Oceans*,  
694 122(3), 1974–1994. <https://doi.org/10.1002/2016JC012228>
- 695 Hermansen, S. C. (2012). *The fate of the Atlantic Water in the North Icelandic Irminger Current*.  
696 University of Bergen.
- 697 de Jong, M. F., Søiland, H., Bower, A. S., & Furey, H. H. (2018). The subsurface circulation of  
698 the Iceland Sea observed with RAFOS floats. *Deep Sea Research Part I: Oceanographic*  
699 *Research Papers*, 141, 1–10. <https://doi.org/10.1016/j.dsr.2018.07.008>
- 700 Jónsson, S., & Briem, J. (2003). Flow of Atlantic water west of Iceland and onto the north

Icelandic shelf. *ICES Marine Science Symposia*, 219, 326–328.

Jonsson, S., & Valdimarsson, H. (2012a). Hydrography and circulation over the southern part of the Kolbeinsey Ridge. *ICES Journal of Marine Science*, 69(7), 1255–1262. <https://doi.org/10.1093/icesjms/fss101>

Jonsson, S., & Valdimarsson, H. (2012b). Water mass transport variability to the North Icelandic shelf, 1994–2010. *ICES Journal of Marine Science*, 69(5), 809–815. <https://doi.org/10.1093/icesjms/fss024>

Jónsson, S. (2007). Volume flux and fresh water transport associated with the East Icelandic Current. *Progress in Oceanography*, 73(3–4), 231–241. <https://doi.org/10.1016/j.pocean.2006.11.003>

Jonsson, Steingrímur, & Valdimarsson, H. (2004). A new path for the Denmark Strait overflow water from the Iceland Sea to Denmark Strait. *Geophysical Research Letters*, 31(L03305), 1–4. <https://doi.org/10.1029/2003GL019214>

Köhl, A., Käse, R. H., Stammer, D., & Serra, N. (2007). Causes of Changes in the Denmark Strait Overflow. *Journal of Physical Oceanography*, 37(6), 1678–1696. <https://doi.org/10.1175/JPO3080.1>

Krauss, W. (1995). Currents and mixing in the Irminger Sea and in the Iceland Basin. *Journal of Geophysical Research*, 100(C6), 10851. <https://doi.org/10.1029/95JC00423>

Kwon, Y.-O., Seo, H., Ummenhofer, C. C., & Joyce, T. M. (2020). Impact of Multidecadal Variability in Atlantic SST on Winter Atmospheric Blocking. *Journal of Climate*, 33(3), 867–892. <https://doi.org/10.1175/JCLI-D-19-0324.1>

Latarius, K., & Quadfasel, D. (2016). Water mass transformation in the deep basins of the Nordic Seas: Analyses of heat and freshwater budgets. *Deep Sea Research Part I: Oceanographic Research Papers*, 114, 23–42. <https://doi.org/10.1016/j.dsr.2016.04.012>

Logemann, K., & Harms, I. (2006). High resolution modelling of the North Icelandic Irminger Current (NIIC). *Ocean Science*, 2(2), 291–304. <https://doi.org/10.5194/os-2-291-2006>

Logemann, K., Ólafsson, J., Snorrason, Á., Valdimarsson, H., & Marteinsdóttir, G. (2013). The circulation of Icelandic waters – a modelling study. *Ocean Science Discussions*, 10(2), 763–824. <https://doi.org/10.5194/osd-10-763-2013>

Macrander, A., Valdimarsson, H., & Jónsson, S. (2014). Improved transport estimate of the East Icelandic Current 2002–2012. *Journal of Geophysical Research: Oceans*, 119(6), 3407–3424. <https://doi.org/10.1002/2013JC009517>

Mastropole, D., Pickart, R. S., Valdimarsson, H., Våge, K., Jochumsen, K., & Girton, J. (2017). On the hydrography of Denmark Strait. *Journal of Geophysical Research: Oceans*, 122(1), 306–321. <https://doi.org/10.1002/2016JC012007>

Mauritzen, C. (1996). Production of dense overflow waters feeding the North Atlantic across the Greenland-Scotland Ridge. Part 2: An inverse model. *Deep Sea Research Part I: Oceanographic Research Papers*, 43(6), 807–835. [https://doi.org/10.1016/0967-0637\(96\)00038-6](https://doi.org/10.1016/0967-0637(96)00038-6)

McCartney, M. S., & Talley, L. D. (1982). The Subpolar Mode Water of the North Atlantic

- 741 Ocean. *Journal of Physical Oceanography*, 12(11), 1169–1188.  
742 [https://doi.org/10.1175/1520-0485\(1982\)012<1169:TSMWOT>2.0.CO;2](https://doi.org/10.1175/1520-0485(1982)012<1169:TSMWOT>2.0.CO;2)
- 743 Oziel, L., Sirven, J., & Gascard, J.-C. (2016). The Barents Sea frontal zones and water masses  
744 variability (1980–2011). *Ocean Science*, 12(1), 169–184. [https://doi.org/10.5194/os-12-169-](https://doi.org/10.5194/os-12-169-2016)  
745 2016
- 746 Pickart, R. S. (1992). Water mass components of the North Atlantic deep western boundary  
747 current. *Deep-Sea Research*, 39(9), 1553–1572.
- 748 Pickart, R. S., Torres, D. J., & Fratantoni, P. S. (2005). The East Greenland Spill Jet\*. *Journal of*  
749 *Physical Oceanography*, 35(6), 1037–1053. <https://doi.org/10.1175/JPO2734.1>
- 750 Pickart, R. S., Spall, M. A., Torres, D. J., Våge, K., Valdimarsson, H., Nobre, C., et al. (2017a).  
751 The North Icelandic Jet and its relationship to the North Icelandic Irminger Current. *Journal*  
752 *of Marine Research*, 75(5), 605–639. <https://doi.org/10.1357/002224017822109505>
- 753 Pickart, R. S., Spall, M. A., Torres, D. J., Våge, K., Valdimarsson, H., Nobre, C., et al. (2017b).  
754 The North Icelandic Jet and its relationship to the North Icelandic Irminger Current. *Journal*  
755 *of Marine Research*, 75(5), 605–639. <https://doi.org/10.1357/002224017822109505>
- 756 Rudels, B., Björk, G., Nilsson, J., Winsor, P., Lake, I., & Nohr, C. (2005). The interaction  
757 between waters from the Arctic Ocean and the Nordic Seas north of Fram Strait and along  
758 the East Greenland Current: results from the Arctic Ocean-02 Oden expedition. *Journal of*  
759 *Marine Systems*, 55(1–2), 1–30. <https://doi.org/10.1016/j.jmarsys.2004.06.008>
- 760 Semper, S., Våge, K., Pickart, R. S., Valdimarsson, H., Torres, D. J., & Jónsson, S. (2019). The  
761 emergence of the north icelandic jet and its evolution from northeast Iceland to Denmark  
762 strait. *Journal of Physical Oceanography*, 49(10), 2499–2521. [https://doi.org/10.1175/JPO-](https://doi.org/10.1175/JPO-D-19-0088.1)  
763 D-19-0088.1
- 764 Smith, W. H. F., & Sandwell, D. T. (1997). Global sea floor topography from satellite altimetry  
765 and ship depth soundings. *Science*, 277(5334), 1956–1962.  
766 <https://doi.org/10.1126/science.277.5334.1956>
- 767 Spall, M. A., & Pedlosky, J. (2008). Lateral Coupling in Baroclinically Unstable Flows. *Journal*  
768 *of Physical Oceanography*, 38(6), 1267–1277. <https://doi.org/10.1175/2007JPO3906.1>
- 769 Swift, J. H., & Aagaard, K. (1981). Seasonal transitions and water mass formation in the Iceland  
770 and Greenland seas. *Deep Sea Research Part A. Oceanographic Research Papers*, 28(10),  
771 1107–1129. [https://doi.org/10.1016/0198-0149\(81\)90050-9](https://doi.org/10.1016/0198-0149(81)90050-9)
- 772 Thurnherr, A. (2018). *How to process LADCP data with the LDEO software*. New York:  
773 Columbia University. Retrieved from  
774 [ftp://ftp.ldeo.columbia.edu/pub/ant/LADCP/UserManuals/how-to/howto\\_2008\\_07\\_09.pdf](ftp://ftp.ldeo.columbia.edu/pub/ant/LADCP/UserManuals/how-to/howto_2008_07_09.pdf)
- 775 Thurnherr, A. M. (2010). A practical assessment of the errors associated with full-depth LADCP  
776 profiles obtained using teledyne RDI workhorse acoustic doppler current profilers. *Journal*  
777 *of Atmospheric and Oceanic Technology*, 27(7), 1215–1227.  
778 <https://doi.org/10.1175/2010JTECHO708.1>
- 779 Le Traon, P. Y., Nadal, F., & Ducet, N. (1998). An Improved Mapping Method of Multisatellite  
780 Altimeter Data. *Journal of Atmospheric and Oceanic Technology*, 15(2), 522–534.  
781 [https://doi.org/10.1175/1520-0426\(1998\)015<0522:AIMMOM>2.0.CO;2](https://doi.org/10.1175/1520-0426(1998)015<0522:AIMMOM>2.0.CO;2)

- Våge, K., Pickart, R. S., Spall, M. A., Valdimarsson, H., Jónsson, S., Torres, D. J., et al. (2011). Significant role of the North Icelandic Jet in the formation of Denmark Strait overflow water. *Nature Geoscience*, 4(10), 723–727. <https://doi.org/10.1038/ngeo1234>
- Våge, K., Pickart, R. S., Spall, M. A., Moore, G. W. K., Valdimarsson, H., Torres, D. J., et al. (2013). Revised circulation scheme north of the Denmark Strait. *Deep-Sea Research Part I: Oceanographic Research Papers*, 79, 20–39. <https://doi.org/10.1016/j.dsr.2013.05.007>
- Våge, K., Moore, G. W. K., Jónsson, S., & Valdimarsson, H. (2015). Water mass transformation in the Iceland Sea. *Deep Sea Research Part I: Oceanographic Research Papers*, 101, 98–109. <https://doi.org/10.1016/j.dsr.2015.04.001>
- Valdimarsson, H., & Malverg, S. (1999). Near-surface circulation in Icelandic waters derived from satellite tracked drifters. *Rit Fiskideildar*, 16, 23–29.
- Vignudelli, S., Snaith, H. M., Lyard, F., Cipollini, P., Venuti, F., Birol, F., et al. (2006). Satellite radar altimetry from open ocean to coasts: challenges and perspectives. *Remote Sensing of the Marine Environment*, 6406. <https://doi.org/10.1117/12.694024>
- Visbeck, M. (2002). Deep velocity profiling using lowered acoustic Doppler current profilers: Bottom track and inverse solutions. *Journal of Atmospheric and Oceanic Technology*, 19(5), 794–807. [https://doi.org/10.1175/1520-0426\(2002\)019<0794:DVPULA>2.0.CO;2](https://doi.org/10.1175/1520-0426(2002)019<0794:DVPULA>2.0.CO;2)
- Yang, J., & Pratt, L. J. (2014). Some Dynamical Constraints on Upstream Pathways of the Denmark Strait Overflow. *Journal of Physical Oceanography*, 44(12), 3033–3053. <https://doi.org/10.1175/JPO-D-13-0227.1>
- Ypma, S. L., Brüggemann, N., Georgiou, S., Spence, P., Dijkstra, H. A., Pietrzak, J. D., & Katsman, C. A. (2019). Pathways and watermass transformation of Atlantic Water entering the Nordic Seas through Denmark Strait in two high resolution ocean models. *Deep Sea Research Part I: Oceanographic Research Papers*, 145(August 2018), 59–72. <https://doi.org/10.1016/j.dsr.2019.02.002>
- Zhao, J., Yang, J., Semper, S., Pickart, R. S., Våge, K., Valdimarsson, H., & Jónsson, S. (2018). A numerical study of interannual variability in the North Icelandic Irminger Current. *Journal of Geophysical Research: Oceans*, 2(9), 2299–2308. <https://doi.org/10.1029/2018JC013800>

**Figure 1.** Schematic representation of the main currents in the vicinity of Iceland: NIIC = North Icelandic Irminger Current; IC = Irminger Current; DWBC = Deep Western Boundary Current; EGC = East Greenland Current; sbEGC = shelfbreak EGC; sEGC = separated EGC; EIC = East Iceland Current; and NIJ = North Icelandic Jet. The hydrographic stations used in this study are indicated by the red circles, comprising 8 transects: FX = Faxaflói, LB = Látrabjarg, KG = Kögur, HB = Hornbanki, SI = Siglunes, MS = Melrakkslétta, LNE = Langanes NE, and LE = Langanes E. The bathymetry is from the GEBCO\_2014 grid. Major topographic features are labeled.

**Figure 2.** (a) Volumetric  $\theta$ -S diagram of all CTD stations, where color denotes the number of measurements within each bin of  $0.2^{\circ}\text{C}$  in temperature and 0.07 in salinity. The domains of the different water masses defined in Table 2 are denoted by the thick black lines. The acronyms are

given in Table 2. (b) Seasonally averaged  $\theta$ -S of the NIIC and NIIC-EIC merged flow (color) per transect (symbols). See the legend. (c) Seasonally averaged  $\theta$ -S of the AW within the current. (d) Same as (c) except for AtOW. Grey dashed lines are the potential density ( $\text{kg m}^{-3}$ ).

**Figure 3.** Mean vertical sections of potential temperature (color,  $^{\circ}\text{C}$ ) overlain by potential density (contours,  $\text{kg m}^{-3}$ ) for the different transects. Station locations and numbers are indicated along the top axis. The bottom topography is from the Smith and Sandwell Global Topography (Smith & Sandwell, 1997). (a) FX, (b) LB, (c) KG, (d) HB, (e) SI, (f) MS, (g) LNE, and (h) LE.

**Figure 4.** Same as Figure 3 except for salinity.

**Figure 5.** Same as Figure 3 except for the 6 transects with absolute geostrophic velocity ( $\text{cm s}^{-1}$ ). (a) FX, (b) LB, (c) KG, (d) HB, (e) SI, and (f) LE. Positive velocities (red) are clockwise currents around Iceland, and negative velocities are counter-clockwise currents. The thick black line is the zero-velocity contour. The names and locations of the currents are indicated at the top of each panel.

**Figure 6.** Vertical sections of percent occurrence of AW (color, %) at each transect overlain by potential density (black and white contours,  $\text{kg m}^{-3}$ ). The red contours ( $\text{cm s}^{-1}$ ) are the mean absolute geostrophic velocities from the 6 transects in Fig. 5, while for transects MS and LN they are the relative geostrophic velocities referenced to the bottom. Positive velocities (solid red contours) are clockwise currents around Iceland, and negative velocities (dashed red contours) are counter-clockwise currents.

**Figure 7.** Same as in Fig. 6 except for percent occurrence of AtOW.

**Figure 8.** (left-hand column) Mean vertical sections of absolute geostrophic velocity from Fig. 5 (color) overlain by the mean values of relative vorticity divided by stretching vorticity (yellow contours; the black contour is the zero value). (right-hand column) Mean vertical sections of Ertel potential vorticity (color). Three transects shown are: KG (panels a and d) and SI (panels b and e) before the NIIC.

**Figure 9.** Maximum and minimum values of relative vorticity divided by stretching vorticity in the NIIC (merged NIIC-EIC) for all occupations of transects LB, KG, HB, SI, (LE). Red (blue) circles are cyclonic (anti-cyclonic) vorticity. The solid lines represent the median values.

**Figure 10.** Lateral maps of mean potential temperature ( $^{\circ}\text{C}$ ) and salinity per season, averaged from the surface to 300 m depth. The thick black line in the temperature and salinity maps represents the approximate boundary between the AW and the PW.

**Figure 11.** Time series of annual mean potential temperature (blue circles,  $^{\circ}\text{C}$ ) where the seasonal signal was removed for each occupation prior to averaging. The standard errors are included. The thick black line is the 12-month low pass. The red line is the linear regression, which is shown only for those cases where the confidence level exceeds 0.9. (a) The NIIC from LB to SI. (b) The NIIC-EIC merged flow at LE. (c) The AW within the NIIC. (d) The AtOW within the NIIC-EIC merged flow.

**Figure 12.** Same as Figure 11 except for salinity.

**Figure 13.** Same as Figure 11 except for volume transport (Sv).

**Table 1.** Number of cruises per transect and season used in the study.

	Winter	Spring	Summer	Fall	total
Faxaflói	21	25	18	22	86
Látrabjarg	12	15	15	15	57
Kögur	16	17	23	16	72
Hornbanki	19	19	13	18	69
Síglunes	20	22	24	19	85
Melrakkaslétta	0	14	4	2	20
Langanes NE	23	27	25	21	96
Langanes E	16	23	15	9	63
Total	127	162	137	122	548

**Table 2.** Water masses definitions following Rudels et al. (2005) and Våge et al. (2011).

Water mass	Acronym	Definition of properties
Surface Water	SW	$T > 3^{\circ}\text{C}$ $\sigma_0 < 27.70 \text{ kg/m}^3$
warm Polar Surface Water	PSWw	$0 \leq T < 3^{\circ}\text{C}$ $\sigma_0 < 27.70 \text{ kg/m}^3$
Polar Surface Water	PSW	$T < 0^{\circ}\text{C}$ $\sigma_0 < 27.70 \text{ kg/m}^3$
Atlantic Water	AW	$T \geq 3^{\circ}\text{C}$ $S > 34.9$
Atlantic-origin Overflow Water	AtOW	$0 \leq T < 3^{\circ}\text{C}$ $\sigma_0 \geq 27.70 \text{ kg/m}^3$ $\sigma_{0.5} < 30.44 \text{ kg/m}^3$
Polar intermediate Water	PIW	$T < 0^{\circ}\text{C}$ $\sigma_0 \geq 27.70 \text{ kg/m}^3$ $S \leq 34.676$
Arctic-origin Overflow Water	ArOW	$T < 0^{\circ}\text{C}$ $\sigma_0 \geq 27.70 \text{ kg/m}^3$ $\sigma_{0.5} < 30.44 \text{ kg/m}^3$
Nordic Seas Deep Water	NDW	$T < 0^{\circ}\text{C}$ $\sigma_{0.5} \geq 30.44 \text{ kg/m}^3$

**Table 3.** NIIC, EIC, and NIIC-EIC merged flow mean absolute geostrophic transports (Sv), including standard errors.

Occupation	Absolute geostrophic transport
FX NIIC	0.80±0.04
LB NIIC	2.24±0.23
KG NIIC	1.16±0.11
HB NIIC	1.37±0.05
SI NIIC	1.43±0.11
SI EIC	1.16±0.08
SI merged	2.59±0.15
LE merged	3.42±0.25

**Table 4:** Net change in potential temperature ( $\theta$ ), salinity (S), and volume transport from 1993 to 2017. Entries with a dash had no significant change.

	$\Delta\theta$ (°C)	$\Delta S$	$\Delta\text{Transport}$ (Sv)
NIIC	0.76	0.08	0.68
NIIC-EIC	0.39	0.05	—
AW	0.44	0.03	0.70
AtOW	—	0.09	—